Unique Amphipathic α-helix Drives Membrane Insertion and Enzymatic Activity of ATG3

Taki Nishimura[1,2,3,5*], Gianmarco Lazzeri[4,5], Noboru Mizushima[2], Roberto Covino[4*], Sharon A. Tooze[3]

[1]PRESTO, Japan Science and Technology Agency, Chiyoda-ku, Tokyo 102-0076, Japan

[2]Department of Biochemistry and Molecular Biology, Graduate School of Medicine, The University of Tokyo, Tokyo 113-0033, Japan

[3]Molecular Cell Biology of Autophagy Laboratory, The Francis Crick Institute, 1 Midland Road, London, NW1 1AT, UK

[4]Frankfurt Institute for Advanced Studies, Ruth-Moufang-Straße 1, Frankfurt am Main 60438, Germany

[5]These authors contributed equally

*Correspondence: Taki Nishimura (ntaki@m.u-tokyo.ac.jp), Roberto Covino (covino@fias.uni-frankfurt.de)

ORCID: Taki Nishimura (0000-0003-4019-5984), Roberto Covino (0000-0003-0884-0402)

1

Abstract

Autophagosome biogenesis requires a localized perturbation of lipid membrane dynamics and a unique protein-lipid conjugate. Autophagy-related (ATG) proteins catalyze this biogenesis on cellular membranes, but the underlying molecular mechanism remains unclear. Focusing on the final step of the protein-lipid conjugation reaction, ATG8/LC3 lipidation, we show how membrane association of the conjugation machinery is organized and fine-tuned at the atomistic level. Amphipathic α-helices in ATG3 proteins (AH$_{ATG3}$) are found to have low hydrophobicity and to be less bulky. Molecular dynamics simulations reveal that AH$_{ATG3}$ regulates the dynamics and accessibility of the thioester bond of the ATG3~LC3 conjugate to lipids, allowing covalent lipidation of LC3. Live cell imaging shows that the transient membrane association of ATG3 with autophagic membranes is governed by the less bulky-hydrophobic feature of AH$_{ATG3}$. Collectively, the unique properties of AH$_{ATG3}$ facilitate protein-lipid bilayer association leading to the remodeling of the lipid bilayer required for the formation of autophagosomes.

(150 words/ Max 150 words)

Teaser

We uncover the unique biophysical property of amphipathic α-helix essential for autophagy

Short title

Unique biophysical property of AH essential for autophagy

Keywords

Autophagy, ATG3, Amphipathic α-helix, LC3 lipidation, Unsupervised machine learning, All-atom MD simulation

2

Introduction

Autophagy is a fundamental cellular event that maintains cellular homeostasis by degrading cytoplasmic materials and damaged organelles. Upon autophagy induction, a cup-shaped membrane structure sequesters a part of cytoplasm and/or selective cargoes by closing to form a double-membrane autophagosome (*1*). Autophagosome formation is driven by the autophagy-related (ATG) proteins and accompanied by dynamic membrane remodeling processes, such as membrane nucleation, expansion and shaping (*2-6*). Several functional groups composed of core ATG proteins play a central role in autophagosome biogenesis: the ULK protein kinase complex, ATG9-containing vesicles, autophagy-specific PI3K (PI3KC3-C1) complex, ATG2-WIPI complex, ATG12–5-16L1 complex, ATG3 and ATG8 proteins (*2, 7*). At the initiation step, multiple ULK complexes are assembled in close apposition to the ER membrane and recruit ATG9 vesicles that act to initiate the seed membrane of the autophagosome precursor. After phosphatidylinositol 3-phosphate (PI3P) generation by PI3KC3-C1 complex, the seed membrane is physically linked to the ER membranes via ATG2-WIPI complex and becomes the destination of ATG2-dependent bulk transport of lipids. Subsequently, membrane lipid imbalance between outer and inner leaflets caused by transferred lipids is equilibrated by the lipid scramblase activity of ATG9 in the nascent autophagosome. This cooperative lipid transport by ATG2 and ATG9, facilitated by a direct interaction between ATG2 and ATG9 (*8*), is thought to induce membrane growth of autophagosomes (*9, 10*). In parallel, ATG8 proteins (LC3s and GABARAPs in mammals) contribute to membrane expansion by different mechanisms. ATG8s undergo lipidation by ATG3 in coordination with the ATG12–5-16L1 complex allowing them to be anchored into autophagic membranes to promote membrane expansion, possibly by inducing membrane hemifusion (*11*) and membrane deformation (*12*). In a recent study, a theoretical model predicts that curvature generation by membrane-shaping proteins including ATG proteins can be a key factor for autophagosome size regulation (*13, 14*).

To accomplish this complicated membrane-mediated process and successfully form autophagosomes, ATG proteins need to interact with membranes in a strictly controlled manner and sense local membrane environments during membrane reorganization. Indeed, ATG proteins have defined spatiotemporal recruitment patterns and specific distributions on autophagic membranes (*15, 16*). This is presumably because each functional group of ATG proteins associates with membranes by a distinct mechanism (*7*). Among lipid-binding modules, amphipathic α-helices (AHs), which sense membrane charge, curvature, unsaturation and lipid composition (*17*), are commonly found in some ATG proteins: ATG14L, VPS34, ATG2, WIPIs, ATG3 and ATG16L1 (*18-22*). Interestingly, PI3KC3-C1 containing ATG14L and VPS34 localizes to both the ER membranes and autophagic membranes (*23,*

24), while ATG2 and ATG12–5-16L1 are detected at the edge of growing phagophores (*13, 25-27*), suggesting that individual AH$_{ATG}$ sense a different membrane environment and have a distinct role in autophagosome formation.

Upon nutrient starvation or autophagy stimulation, ATG8/LC3 proteins undergo lipidation by the E1-E2-E3-like enzymatic cascade. The E2-like ATG3 directly binds to membranes via its N-terminal AH$_{ATG3}$ to transfer ATG8/LC3 to phosphatidylethanolamine (PE) (*22, 28, 29*) by bimolecular nucleophilic substitution SN2 reaction (**Fig. S1A**) (*30, 31*). As the AH$_{ATG3}$ shows a preference for highly curved membranes *in vitro* (*32*) and AH$_{ATG3}$ is indispensable for LC3 lipidation (*22*), ATG3 could execute LC3 lipidation on highly curved autophagic membranes. Despite such findings, how ATG3 recognizes membrane lipids via its AH$_{ATG3}$ and the dynamics of ATG3 on autophagic membranes are poorly understood. Whether membrane binding and curvature sensing are the exclusive functions of AH$_{ATG3}$ in autophagy is still unresolved. In fact, ATG16L1, a component of the E3-like ATG12–5-16L1 complex, is a dominant factor for curvature sensing among the components of LC3 conjugation machinery (*19, 33*), implying that AH$_{ATG3}$ has another pivotal function in addition to membrane anchoring (*34*).

To address the function of ATG3 in autophagy we focused our studies on the essential lipid binding module AH$_{ATG3}$. Unsupervised machine learning analysis of more than 1800 AHs revealed that ATG3-type AHs contain less hydrophobic and less bulky amino acids compared to unrelated AHs. This biophysical feature of AH$_{ATG3}$ is highly conserved from yeast to mammals, and it is required for ATG3 to achieve efficient LC3 lipidation in cells. Molecular dynamics (MD) simulations of ATG3~LC3 intermediate showed that the biophysical features of AH$_{ATG3}$ are fine-tuned to regulate its dynamics and substrate accessibility. Moreover, live cell imaging analysis revealed transient membrane association of ATG3 with autophagic membranes, which is governed by the less-hydrophobic feature of AH$_{ATG3}$. Here, ATG3's AH fine-tuned biophysical features are fundamental to its central role in the ATG3 enzymatic reaction by organizing ATG3~LC3 conjugate on membranes. We propose that the conceptual and technical framework we present here can serve as a general platform to better understand the role of AHs in regulating key phenomena in the cell.

Results

The essential function of AH_{ATG3} for LC3 lipidation is conserved among species

To investigate the sensitivity of AH_{ATG3} to membrane curvature, we first performed circular dichroism (CD) experiments with a peptide corresponding to the N-terminal 22 aa residues of the human ATG3 sequence ($ATG3_{1-22}$ peptide) that contains an amphipathic α-helix AH_{ATG3}. Consistent with a recent report (*32*), the peptide was unfolded both in aqueous solution and in the presence of extruded DOPC/DOPE liposomes ($\geqq$100 nm diameter), while its CD spectrum demonstrated the characteristic shape of an α-helix in the presence of sonicated liposomes (~38 nm diameter) under high protein/lipid ratio (1:80) conditions (**Fig. 1A and B**). We also checked the effect of anionic phospholipids on an α-helical conformation of the $ATG3_{1-22}$ peptide by using sonicated liposomes. Compared to DOPC/DOPE liposomes, anionic phospholipids, such as phosphatidylinositol (PI), phosphatidylserine (PS) and phosphatidic acid (PA), slightly promoted the α-helical conformation of the $ATG3_{1-22}$ peptide (**Fig. S1B and S1C**). These results indicate that AH_{ATG3} has the ability to interact with highly curved membranes with a preference for charged membranes *in vitro*.

To assess whether the membrane binding via AH is sufficient for AH_{ATG3} function *in vivo*, we designed a rescue assay by using ATG3 chimeras in *ATG3* KO MEF cells (**Fig. 1C**). We replaced the AH_{ATG3} region (1-18 aa) with other AHs (*18, 20, 35, 36*) and made various ATG3 chimeras. All constructs kept the key residues P21 and L23 that are critical for LC3 lipidation (*32*) in the conserved region following AH_{ATG3} (**Fig. 1C**). To avoid N- or C-terminal tagging of ATG3 which might interfere with ATG3's function, we inserted a GFP tag into the middle region of ATG3 (ATG3-inGFP) by following previous work (*37*). To check LC3 flux upon starvation, the cells were cultured under fed or starved conditions with and without lysosomal inhibitor bafilomycin A_1 ($BafA_1$). In this experiment, ATG3-inGFP restored LC3 lipidation under fed conditions and LC3-II accumulation in the presence of $BafA_1$, indicating that ATG3-inGFP was fully functional in cells. In contrast, ATG3 chimeras carrying AHs derived from VPS34, ATG14L, ATG2A, NUP133 or Spo20, did not efficiently rescue LC3 lipidation (**Fig. 1D and S1D**). In line with this, LC3 puncta formation upon starvation was restored in the cells expressing ATG3 but not in the cells expressing the ATG3 chimeras (**Fig. 1E and S1E**). Intriguingly, the ATG3 did not show clear punctate structures, while AH_{VPS34}, AH_{ATG14L}, AH_{NUP133}, and AH_{Spo20} chimeras showed a membrane localization and/or puncta formation (**Fig. 1E, arrowheads**). ATG3 chimera carrying AH_{ATG2A} co-localized with a few small LC3 puncta in some cells, but the puncta size was much smaller than those observed in the cells expressing ATG3 WT. These data indicate that the membrane targeting of ATG3 via any other AH is not enough for ATG3 to efficiently execute LC3 lipidation reaction.

5

Alternatively, ATG3 chimeras carrying AH derived from other species' ATG3 clearly restored LC3 lipidation (**Fig. 1F**). AH$_{DmATG3}$ and AH$_{ScATG3}$, which are AHs of *Drosophila melanogaster* Atg3 and *Saccharomyces cerevisiae* Atg3, respectively, induced LC3 lipidation as much as AH$_{ATG3}$ (**Fig. S1F**). LC3 puncta formation was restored in these cells as well (**Fig. 1E and S1E**). In the cells expressing ATG3 chimera carrying AH$_{SpATG3}$ derived from *Schizosaccharomyces pombe* Atg3, impaired LC3 lipidation and puncta formation were efficiently rescued (**Fig. 1E, 1F, S1E and S1F**). Collectively, these findings suggest that a key function of AH$_{ATG3}$, which cannot be substituted by unrelated AH$_{non-ATG3}$, is conserved in ATG3 proteins.

Unsupervised machine learning reveals the unique biophysical identity of AH$_{ATG3}$

We searched for common features of AHs derived from ATG3 proteins by comparing sequences of various AHs. ATG3-type AHs have multiple charged and uncharged polar residues and the positively charged residues (K and R) are located at the hydrophilic/hydrophobic interface (**Fig. 2A**). On the other hand, glycine (G) and serine (S) residues are enriched in the hydrophilic faces of AH$_{ATG14L}$ and AH$_{NUP133}$. AH$_{Spo20}$ has a large hydrophilic face composed of many positively charged residues, while AH$_{ATG2A}$ contains many hydrophobic residues. AH$_{VPS34}$ has several charged residues like AH$_{ATG3}$, while it is longer than AH$_{ATG3}$ (**Fig. 2B**). To systematically identify distinct features of AH$_{ATG3}$ conserved among species, we collected homologue sequences of proteins carrying AHs used in the rescue assay (**Fig. 1**), obtained the sequences of their AH region and calculated the amino acid composition and physicochemical properties based on the HeliQuest algorithm (see Materials and Methods) (*38*). Then, we analyzed the dataset of AH parameters using machine learning approaches (**Fig. 2C**). In this analysis, we classified ATG3-type AHs into five groups by phylum: Chordata, Arthropoda, Nematoda, Streptophyta and Ascomycota.

We first compared the relative amino acid composition in a heat map (**Fig. S2A**) and noticed that bulky hydrophobic tryptophan (W) residues are rarely found in ATG3-type AHs. Instead, they are rich in small hydrophobic valine (V) residues. Another feature of ATG3-type AHs is a zwitterionic hydrophilic face composed largely of multiple charged and uncharged polar residues. We next investigated ATG3-type AHs by analyzing the dataset of AA composition and AH parameters. To interpret the high-dimensional data, we used 3D-Principal Component Analysis (PCA). PCA efficiently separated ATG3-type AH from AH$_{ATG2}$, AH$_{VPS34}$, AH$_{NUP133}$ and AH$_{Spo20}$ (**Fig. 2D**). The first principal component, PC1, strongly correlates with the number of hydrophobic AA residues, such as the number of apolar residues and bulky hydrophobic residues (**Fig. 2E**). Positive and negative values of PC2

6

correlate with the number of charged residues and mean hydrophobicity, respectively. PC3 corresponds to the number of glycine (G) residues (**Fig. 2E**). Based on this PCA analysis, we replotted all AHs based on their number of bulky AA and glycine residues, and mean hydrophobicity (**Fig. S2B**). The replotted data showed that ATG3-type AHs are characterized by a lower hydrophobicity, and fewer bulky and glycine residues (**Fig. 2F and S2C**). On the other hand, Chordata AH_{ATG14L} were distributed into the same cluster with ATG3 type AHs in this analysis (**Fig. 2D**). The inability of the ATG3-AH_{ATG14L} chimera to execute LC3 lipidation might be due to the difference in regional effects rather than overall biophysical parameters.

Low hydrophobicity and a low number of bulky-hydrophobic residues of AH_{ATG3} are crucial for efficient LC3 lipidation

Considering that ATG3 needs to be recruited to membranes to execute LC3 lipidation, the features of AH_{ATG3} —low hydrophobicity and scarce bulky hydrophobic residues— are relatively counterintuitive. Therefore, we investigated whether these AH_{ATG3} features are necessary ATG3's function in autophagy. We mutated the AH_{ATG3} to introduce hydrophobic residues and performed the LC3 rescue assays. AH_{ATG3} mutants enriched in bulky-hydrophobic residues (3W, 2W and 5W) were prepared by replacing small hydrophobic residues of AH_{ATG3} with bulky tryptophan residues (**Fig. 3A**). The 3W mutant restored LC3 lipidation flux as much as ATG3 WT. In contrast, the 2W and 5W mutants showed less and nearly no LC3 lipidation, respectively (**Fig. 3B and 3C**). LC3 puncta formation was observed in the cells expressing the 3W mutant, whereas smaller punctate structures were formed and the number of LC3 puncta was much less in the cells expressing the 5W mutant (**Fig. 3D and 3E**). These results indicate that increasing both hydrophobicity and the number of bulky residues in AH_{ATG3} is detrimental to ATG3 function *in vivo*. To further validate the significance of the unique biophysical property of AH_{ATG3}, we checked the effect of manipulation on the hydrophobic face of AH in the rescue assay. Among AHs used in this study, AH_{ATG2A} shows extremely high hydrophobicity (**Fig. 2G**) and this chimera containing AH_{ATG2A} was not functional in *ATG3* KO cells (**Fig. 1**). The bulky hydrophobic residues (W and F) of AH_{ATG2A} were mutated into valine residues to reduce its hydrophobicity and the number of bulky residues (**Fig. 3A**). In the rescue assay, the AH_{ATG3} chimera carrying less bulky-hydrophobic $AH_{ATG2A-m1}$ significantly restored LC3 lipidation flux and LC3 puncta formation (**Fig. 3D-G**). Thus, the reduction of bulky-hydrophobic residues in the chimeric AH_{ATG2} resulted in a positive impact on ATG3 function.

Given the relative contribution of the hydrophilic face of AH_{ATG3} on its hydrophobicity, we also examined whether mutations on polar residues affect AH_{ATG3} function (**Fig. S3A**). Replacing either charged (4A mutant) or uncharged polar residues (NTQ-A mutant) did not

apparently interfere with LC3 lipidation flux upon starvation (**Fig. S3B and S3C**). Consistently, LC3 puncta formation was clearly observed in the cells expressing the mutants as well as those observed in the expressing ATG3 WT (**Fig. S3D and S3E**). In contrast, the 8A mutant, lacking all polar residues in the hydrophilic face of AH$_{ATG3}$ (**Fig. S3A**), restored neither LC3 lipidation nor LC3 puncta formation (**Fig. S3B-E**), suggesting that overall hydrophilicity (and hydrophobicity as well) of AH$_{ATG3}$ is crucial for ATG3 function rather than some specific polar residues. All together, these data revealed that the defining features of AH$_{ATG3}$ are functionally important in LC3 lipidation reaction.

MD simulations reveal the dynamics of the ATG3~LC3 conjugate on the membranes

To study the molecular interaction of ATG3 with membranes during LC3 lipidation reaction, we ran molecular dynamics (MD) simulations and investigated the dynamics of the ATG3~LC3 conjugate on model membranes. MD simulations produce trajectories that display the dynamics of molecular systems with atomistic details resulting from a physics-based model. In this way, these simulations can provide insight into how dynamics leads to molecular mechanisms of ATG3-dependent LC3–PE conjugation and how these are affected by perturbations of the WT system.

MD simulations require a structure of the complex as initial information. Without an experimentally determined structure, we modeled the complex with AlphaFold (*39*). The five structures predicted by AlphaFold were similar (**Fig. S4A**). ATG3's N-terminal was still folded as an α-helix in these models, connecting via a short linker to the body part of ATG3 containing a large, disordered region. LC3 formed a complex with ATG3 possibly via the LC3 interacting region (LIR) of ATG3 (*40*), and we additionally modeled the thioester bond between CYS264 of ATG3 and GLY120 of LC3. We inserted the Alpha Fold model into a solvated lipid bilayer and ran long equilibrium MD simulations. The simulated complex remained folded and stably inserted into the bilayer.

The ATG3~LC3 conjugate was highly dynamic and ranged between conformations where LC3 was pointing upwards fully solvated and those bound to the membrane (**Fig. 4A and 4B**). In the initial Alpha Fold model, LC3 pointed away from the membrane, not forming any contact with the membrane (**Fig. 4C**). Its path toward the membrane was sterically hindered by one of ATG3's disordered regions (125aa-197aa) including the flexible region (89-193aa) (*41-43*) and ATG12-interacting region (153-165aa) (*42, 43*). The disordered region was pointed downwards and charged residues such as GLU170 in the region could form contacts with individual lipids (**Fig. 4C**), tethering the whole region to the bilayer ("LC3-UP/Disordered-DOWN" conformation). ATG3's N-terminal AH was dynamic throughout all

simulations but remained folded and inserted in the membrane (**Fig. S4B**).

In our simulations, the complex also spontaneously reorganized to an alternative arrangement, where ATG3's disordered region pointed upwards and made way for LC3 to approach the bilayer ("LC3-DOWN/Disordered-UP" conformation) (**Fig. 4D and 4E**). In this conformation, LC3 formed long-lasting interactions with lipids in the bilayer. Notably, CYS264 of ATG3 and GLY120 of LC3, connected by the thioester bond, formed a prolonged contact (approx. 400 ns) with a PE headgroup. Additionally, the region around ATG3's catalytic CYS264 engaged in extended contacts with the lipids (**Fig. 4F**). Most of the lipid interacting residues are relatively conserved (**Fig. S4C, asterisks**), implying that the molecular mechanisms of how ATG3~LC3 conjugate interacts with membranes might be conserved across species.

AH_{ATG3} regulates the organization of ATG3~LC3 conjugate on membranes

We wondered how mutations in the AH would affect its dynamics and the organization of the ATG3~LC3 conjugate. We created an atomistic model of the first 24 residues of ATG3 as an α-helix and inserted it into a lipid bilayer (**Fig. 5A**). Studying the helix in isolation enabled us to focus on the helix-membrane interactions and accumulate longer simulation times. As in the complex, the helix was dynamic but remained inserted and folded during cumulative 30 µs long MD simulations. The helix was localized at the interface between the bilayer's headgroup region and water. Its hydrophobic residues pointed towards the core of the membrane, whereas the polar and charged residues flanked it or pointed upwards. Flanking residues formed short-lived interactions with lipid head groups. While dynamic, the N-terminus inserted, on average, more deeply into the bilayer than the helix's C-terminal part. In a control MD simulation, the same α-helix model in water rapidly unfolded (**Fig. S5**), confirming that the N-terminal region of ATG3 needs to be inserted into a lipid bilayer to form an amphipathic helix.

We considered the atomistic model of the AH inserted in a lipid bilayer and mutated five residues to W (**Fig. 5B**). The 5W mutation, which cannot rescue, remained stably folded and inserted in a different organization in the bilayer during a 3 µs long MD simulation. We quantified the different placements in the bilayer by comparing the distribution of tilt angle alpha of the WT and 5W AHs (**Fig. 5C**). Alpha is the angle formed between the axis of the AH and the XY plane identified by the membrane. For both helices, alpha was highly dynamic over approximately 30 degrees. However, there was a significant difference between WT and 5W: While the former formed, on average, a 5.0 ± .0 deg angle—the helix pointed upwards from the N- to the C-terminus—the latter formed a negative angle, -2 ± 1 deg.

The 5W AH affected the organization of the whole ATG3~LC3 conjugate and its

interactions with the membrane. We simulated the complex containing a 5W mutated AH in the LC3-UP and LC3-DOWN conformations. In the first case, there were no significant differences with the WT-LC3 complex in the analogous conformation. Instead, comparing WT and 5W in the LC3-DOWN conformation showed LC3 and its lipidation site appeared slightly rotated (**Fig. 5D and 5E**). Additionally, the 5W-LC3 complex displayed a more heterogeneous organization. The five simulations of the WT in the LC3-DOWN conformation we ran did not reorganize and remained in contact with the membrane (**Fig. 5F**). On the contrary, out of the five simulations ran with the 5W-LC3-DOWN conformation, two significantly rearranged. The soluble part of the complex lost contacts with the AH decreasing its interactions with the membrane (**Fig. 5G and 5H**).

Transient membrane association of ATG3 is governed by AH$_{ATG3}$ *in vivo*

We observed that ATG3 WT did not show clear membrane localization in the rescue assay (**Fig. 1E**). Therefore, we hypothesized that the membrane association of ATG3 might be transient. To validate this possibility, we analyzed ATG3-inGFP dynamics in live cells under starved conditions using a Deltavision microscope. As LC3 was unavailable as an autophagosome marker in *ATG3* deficient cells, Halo-tagged ATG5 was used to visualize autophagic membranes instead. Under starved condition with Halo-ligands, Halo-ATG5 puncta gradually appeared and then disappeared within a few minutes in ATG3-inGFP-expressing *ATG3* KO cells (**Movie 1**). On the other hand, ATG3-inGFP was diffusely distributed in the cytoplasm and the fluorescence signal peaks were not clearly observed on Halo-ATG5-positive structures (**Fig. 6A and 6B**). In some cases (~4.44%), an enrichment of ATG3-inGFP fluorescence signals on Halo-ATG5 puncta was detected (**Fig. 6A, 6B**, **and Movie 2**). We imaged the cells expressing ΔAH mutant and analyzed more than 100 Halo-ATG5 puncta in live cells, but there was no correlation of ΔAH mutant with Halo-ATG5 (**Fig. 6C, 6F, and Movie 3**), confirming that ATG3-inGFP is targeted to autophagic membranes dependent on its AH$_{ATG3}$. These results suggest that a small amount of ATG3 is sufficient to achieve LC3 lipidation reaction though it cannot be easily visualized by fluorescent microscopy. In contrast, ATG3 chimeras carrying a bulky-hydrophobic rich AH$_{ATG3}$ mutant often formed punctate structures on Halo-ATG5 puncta (**Fig. 6D and 6E**). Both 3W and 5W mutants were recruited to punctate structures synchronously with Halo-ATG5 puncta formation (**Movies 4 and 5**). Live imaging analysis showed that ~40.9% and ~80.9% of Halo-ATG5 puncta were co-localized with 3W and 5W mutants, respectively (**Fig. 6F**). In addition, 5W clearly localized in reticular membrane structures and stayed there even after the disappearance of Halo-ATG5 structures (**Movie 5**), indicating that 5W mutant localizes to non-autophagic membranes in addition to autophagic membranes and that the dissociation

10

of ATG3-inGFP 5W from these membranes is significantly delayed. Collectively, these results suggest that ATG3 dynamics is governed by low hydrophobic and less bulky AH, which ensures efficient ATG3 enzymatic reaction and recycling.

Discussion

Our findings converge to support a model of AH$_{ATG3}$-mediated LC3 lipidation reaction on autophagic membranes (**Fig. 6G**). ATG3~LC3 conjugate can be recruited to autophagic membranes via the membrane association of AH$_{ATG3}$. In this state, LC3 is pointing upwards and does not interact with the membrane due to the steric hindrance by the ATG3 disordered region (**Fig. 4**). Given that ATG3 interacts with ATG12, a component of the E3-like ATG12–5-16L1 complex, via its ATG12-binding region in the disordered region (**Fig. S4C**) (*42, 43*), a conformational change of ATG3~LC3 conjugate from "LC3-UP/Disordered-DOWN" to "LC3-DOWN/Disordered-UP" might be facilitated by the interaction of ATG3 with ATG12–5-16L1. While previous data (*41, 42, 44*) has suggested a mechanism for how ATG3 enzymatic activity is promoted by ATG12–5-16L1, our observations support an alternative mechanism. Subsequent to the movement of the disordered region, the CYS-GLY thioester bond of ATG3~LC3 conjugate gets closer to the lipid head group forming an ATG3~LC3–PE intermediate. Once LC3 GLY120 forms an amide bond with an amino group of PE, ATG3 promptly dissociates and goes to the next round (**Fig. 6G, left**). This highly dynamic property of ATG3 is determined by the unique biophysical fingerprint of AH$_{ATG3}$ (**Fig. 1-3**). In the case of the high bulky-hydrophobic 5W mutant, ATG3 targets autophagic membranes, is stalled on the membranes and cannot leave efficiently. MD simulation suggests that 5W mutation interferes with the organization and stability of ATG3~LC3 conjugate in the state of LC3-DOWN conformation (**Fig. 5**), resulting in less lipidation (**Fig. 3B, 3C and 6G, right**). From these findings, we propose that AH$_{ATG3}$ plays a central role in ATG3 enzymatic reaction by organizing the overall structure of ATG3~LC3 conjugate on membranes and the unique properties of the AH ensure a transient membrane association of ATG3.

Based on the biochemical activity of ATG3 *in vitro* experiments, it has been previously proposed that AH$_{ATG3}$ serves as a curvature sensor in LC3 lipidation reaction (*22*). But, contrary to this assumption, membrane curvature-sensing AHs, such as AH$_{ATG14L}$ and AH$_{NUP133}$, were not functional in the *ATG3* KO rescue assay (**Fig. 1**), indicating that *in vivo* function of AH$_{ATG3}$ is neither just a membrane anchor nor curvature sensing. Then, how does AH$_{ATG3}$ positively contribute to ATG3 enzymatic reaction? One possible scenario is that dynamic interaction of AH$_{ATG3}$ with membranes could allosterically control the structure of ATG3~LC3 conjugate together with the disordered region (*42*), thus regulating substrate accessibility to the CYS-GLY thioester bond. Another possibility is that AH$_{ATG3}$ might serve as a transient component of the catalytic triad. As we observed that AH$_{ATG3}$ almost reaches both the CYS-GLY thioester bond and PE lipids in the simulation (**Fig. 5F**), AH$_{ATG3}$ might be able to organize the hydrogen bond network with the thioester bond and PE head group during LC3 lipidation reaction, which will promote the deprotonation of PE amino group and the

formation of oxyanion hole (**Fig. S1A**). These mechanistic aspects need to be scrutinized in a future study. Recently, it has been reported that ubiquitin can be conjugated to PE (*45*) as well as Atg8/LC3. However, we could not find an AH in the E2 enzyme for PE ubiquitination. As the E3 enzyme involved in the ubiquitin–PE conjugation is a membrane-spanning protein, the ubiquitin transfer cascade for PE lipids might use a distinct mechanism from ATG3-dependent LC3 lipidation reaction.

So far there have been no reported structures for the ATG3~LC3 conjugate due to the arduous task of the conjugate purification and its intrinsic instability. To overcome this technical issue, we took advantage of AlphaFold model to obtain a predicted structure of ATG3~LC3 conjugate. To our knowledge, this is the first study to analyze membrane association of the ATG3~LC3 conjugate *in silico* and show the possibility that its CYS-GLY thioester bond can form a long-lasting contact with lipid head groups. As several residues around the catalytic active site (LYS208, TYR210, ARG214, and ARG265) show the interaction with lipids within a narrow region together with the CYS-GLY thioester bond, these residues could be at play in the enzymatic reaction. In addition, the disordered region (ARG135, GLU170) of ATG3 and the N-terminal region (LYS5) of LC3 are associated with the membranes. Consistently, the lipidated LC3 N-terminus has been shown to interact with liposomes *in vitro* and *in silico* (*14*). These weak membrane associations might work in a concerted manner, in tandem with the ATG16L1 and WIPI2 proteins (*33*), to facilitate LC3 lipidation and/or autophagosome biogenesis.

Accumulating evidence shows that some other ATG proteins have functional AHs. The requirement for an amphipathic region and the dependency on membrane curvature *in vitro* have been investigated in previous studies. However, it is still enigmatic how AH$_{ATG}$ contribute to autophagy *in vivo*, partly because our knowledge on the physicochemical properties of AH$_{ATG}$ essential for autophagy is very limited. Indeed, the gap between *in vitro* and *in vivo* experiments makes it difficult to assess AH$_{ATG}$ biological functions. In this study, we revealed that AH$_{ATG3}$ are characterized as being less bulky-hydrophobic compared to other AHs, and this property is essential for its *in vivo* function. Given that bulky hydrophobic residues increase the membrane penetration activity of AHs, membrane association mediated by AH$_{ATG3}$ might be energetically advantageous for the repetitive lipidation reactions required to decorate the membrane with lipidated ATG8 proteins. It would be important, and indeed as our work shows, essential to investigate the dedicated function of each AH$_{ATG}$ based on their unique properties of each AH$_{ATG}$ to deepen the understanding of the relationship between ATG proteins and membrane lipids.

Fine-tuning the relationship between structure at the atomistic resolution, membrane lipid composition, and dynamics could be a general feature for AHs involved in cellular

13

processes (*46, 47*). We propose to move beyond simplified models, which are based exclusively on one biophysical property, to a more nuanced understanding of the role played by AHs. From this point of view, comparative analysis of AHs with unsupervised machine learning will be a powerful approach for the identification of multiple key properties conserved among species. Moreover, we showed that the dynamics of the AH_{ATG3} in the membrane controls the structural dynamics of the whole complex. The perturbation induced by mutating amino acids in AH_{ATG3} could also be mimicked by changing the composition of the lipids that surround the helix. AHs and their host membranes co-evolved to enable fundamental cellular functions and should be studied with a holistic approach (*48*).

Materials and Methods

Plasmids

Descriptions of plasmids used in this study are provided in Table S1. cDNAs encoding the full length of human ATG3 (NP_071933) and mouse ATG5 (NP_444299) were amplified by PCR and subcloned into pMRX-IP and pMRX-IPU-HaloTag7 backbone vectors, respectively. pMRX-IP-hATG3$_{1-125}$-EGFP-hATG3$_{126-314}$ was generated by inserting the sequence coding EGFP into between E125 and I126 of ATG3. For generation of ATG3 chimeras carrying AH derived from other proteins, two overlapping oligonucleotide primers coding AH of interest were annealed and elongated by a single PCR reaction. Subsequently, the purified PCR products were inserted by seamless DNA cloning method (*49*). ySpo20$_{57-77aa}$ (NP_013730), hNUP133$_{245-265aa}$ (NP_060700), hVPS34$_{864-867aa}$ (NP_002638), hATG14L$_{471-488aa}$ (NP_055739), hATG2A$_{1750-1767aa}$ (NP_055919), *Drosophila melanogaster* Atg3$_{1-18aa}$ (NP_649059), *Saccharomyces cerevisiae* Atg3$_{1-12aa}$ (NP_014404), and *Schizosaccharomyces pombe* Atg3$_{1-15aa}$ (NP_596664) were described as AH$_{Spo20}$, AH$_{NUP133}$, AH$_{VPS34}$, AH$_{ATG14L}$, AH$_{ATG2A}$, AH$_{DmATG3}$, AH$_{ScATG3}$, and AH$_{SpATG3}$, respectively. All deletion and point mutation mutants of ATG3 were generated by a PCR-based method.

Antibodies and reagents

Antibodies used for immunoblotting are listed: rabbit polyclonal anti-LC3 (#1) (*50*), mouse monoclonal anti-HSP90 (BD Transduction Laboratories, 610419), rabbit polyclonal anti-GFP (Invitrogen, A6455), Secondary antibodies are HRP-conjugated anti-rabbit IgG (Jackson ImmunoResearch Laboratories, 111-035-144), HRP-conjugated anti-mouse IgG (Jackson ImmunoResearch Laboratories, 315-035-003). Antibodies used for immunofluorescence are as listed: rabbit polyclonal anti-LC3 (MBL, PM036, lot 025) and AlexaFluor 568-conjugated anti-rabbit IgG (Invitrogen, A-11036). All lipids were purchased from Avanti: DOPC (850375C), DOPE (850725C), Liver PI (840042C), DOPS (840035C) and DOPA (840875C). Bafilomycin A$_1$ (#11038) was purchased from Cayman.

Circular dichroism (CD) spectroscopy

The peptide containing ATG3 N-terminal region (MQNVINTVKGKALEVAEYLTPVWK) was synthesized by the Francis Crick Peptide Chemistry Technology Platform. Lipids were mixed at the desired ratio, dried under argon and placed in a rotary evaporator to completely remove the organic solvent. The lipid films were rehydrated and resuspended in buffer A (10mM Tris-HCl pH 7.5, 150mM KCl). The suspension was frozen and thawed 5 times using liquid nitrogen and a water bath, and then extruded through 0.2 μm or 0.1 μm membrane

15

(Whatman) using a Mini-Extruder (Avanti Polar Lipid). Very small liposomes were prepared by sonication on ice with a tip sonicator (Misonix). Lipid debris were removed by 25,000 x*g* for 20 min. The size of liposomes was checked by Zetasizer Nano ZS (Malvern Instruments). For CD spectra measurement, the ATG3 peptide (final conc. 75 μM) was mixed with 6 mM liposome solution and analyzed using a Jasco J-815 spectrometer with a quartz cell of 0.02 cm path length. Each spectrum is the average of 50 scans recorded from 190 to 260 nm, with a bandwidth of 2 nm, a step size of 0.2 nm and a scan speed of 200 nm min^{-1}. The buffer contribution was subtracted. The α-helix content was calculated from the molar ellipticity at 222 nm ($[\partial]_{222 \text{ nm}}$) according to: % α-helix ($[\partial]_{222 \text{ nm}}$+2340)/303 (*36*).

Cell lines and culture conditions

Authenticated HEK293T cells were used in this study. *Atg3* KO MEF was generated previously (*51*). Cells were maintained in Dulbecco's Modified Eagle Medium (Wako, 043-30085) supplemented with 10% fetal bovine serum (Sigma-Aldrich, 173012) in a 5% CO_2 incubator at 37 °C. *Atg3* KO MEF stably expressing ATG3 WT or ATG3 chimera were generated as follows: HEK293T cells were transfected using Lipofectamine 2000 reagent (Thermo Fisher Scientific, 11668019) with retroviral plasmid, pCG-VSV-G and pCG-gag-pol, following which the medium was replaced with fresh medium. After 3 days, the culture medium was collected and filtered with a 0.45 μm filter unit (Millipore, SLHVR33RB). *Atg3* KO MEFs were treated with the retrovirus containing medium and 8 μg/mL polybrene (Sigma-Aldrich, H9268). After 2 days, drug selection was performed with 3 μg/mL puromycin (Sigma-Aldrich, P8833). Subsequently, GFP-low expressing cells were sorted by flow cytometry (Sony, SH800).

Immunoblotting

Cells were cultured under DMEM supplemented with FBS or DMEM without amino acids (Wako, 048-33575) in the absence or presence of 100 nM bafilomycin A$_1$ for 6 h, and then collected in ice-cold PBS by scraping on ice. The precipitated cells were suspended in 100 μl lysis buffer (25 mM Hepes-NaOH, pH7.5, 150 mM NaCl, 2 mM MgCl$_2$, 0.2% n-dodecyl-b-D-maltoside [nacalai, 14239-54] and protease inhibitor cocktail [nacalai, 03969-34]) and incubated on ice for 20 min.   Ninety μl of cell lysates were mixed with 10 μl of lysis buffer containing 0.1 μl benzonase (Merck Millipore, 70664) and further incubated on ice for 15 min. The remaining cell lysates were centrifuged at 17,700 x *g* for 15 min and the supernatant was used to measure protein concentration by NanoDrop One spectrophotometer (Thermo Fisher Scientific). The cell lysates were mixed with SDS-PAGE sample buffer and heated at 95°C for 5 min. Samples were subsequently separated by SDS-PAGE and transferred to

Immobilon-P PVDF membranes (Merck Millipore, IPVH00010) with Trans-Blot Turbo Transfer System (Bio-Rad). After incubation with the indicated antibodies, the signals from incubation with SuperSignal West Pico PLUS Chemiluminescent Substrate (Thermo Fisher Scientific, 34580) was detected with Fusion Solo S (VILBER). Band intensities were quantified with Fiji.

Fluorescence microscopy

Cells grown on coverslips were fixed with 4% paraformaldehyde in PBS for 20 min, permeabilized with 50 µg/ml digitonin (Sigma-Aldrich, D141) in PBS for 5 min, blocked with 3% BSA in PBS for 30 min. After incubation with the indicated antibodies, the specimens were mounted in SlowFade with DAPI (Invitrogen, S36939) and observed using a confocal FV3000 confocal laser microscope system (Olympus). For the final output, images were processed using Adobe Photoshop 2021 v22.5.9 software (Adobe). The number of LC3 puncta was counted using Fiji. Briefly, the images were applied with a Gaussian filter for noise suppression and processed with Top-Hat filter. After setting threshold and watershed segmentation, the number of LC3 puncta were counted by Analyze Particles command. Cells were counted by using Cell Counter plug-in. Microcopy and image analysis were done blind.

Live imaging analysis

ATG3 KO MEFs stably expressing ATG3-inGFP, mRuby3-LC3 and Halo-ATG5 were grown on a glass bottom dish (IWAKI, 3910-035). The cells were washed twice with PBS and incubated in starvation medium with 200 nM SaraFluor 650T ligand. Images were acquired with a 60× PlanAPO oil-immersion objective lens (1.42 NA; Olympus), using a Deltavision microscope system (GE Healthcare) coupled with an Olympus IX81-ZDC and a cooled CCD camera CoolSNAP HQ2 (Photometrics, Tucson). During live-cell imaging, the culture dish was mounted in a chamber INUB-ONI-F2 (TOKAI HIT) to maintain the culture conditions (37°C and 5% CO_2). ATG3-inGFP, mRuby3-LC3B and Halo-ATG5 were illuminated with a mercury arc lamp attenuated to 10, 32 and 32% by neutral density filters, respectively. Exposure times were 0.6 s for ATG3-inGFP, 0.6 s for mRuby3-LC3B and 0.4 s for Halo-ATG5. Time-lapse images were acquired at 30-s intervals. Deconvoluted images were obtained using softWoRx software. To analyze ATG3 puncta formation on autophagic membranes, the area containing ATG5-positive puncta in time-series image stacks were selected, converted to an intensity map using the Fire lookup table and then aligned into a single montage image using Fiji. For the final output, images were processed using ImageJ and Adobe Photoshop 7.0.1 software.

AH data analysis

17

We collected 1886 protein sequences containing an AH across different species in HMMER web server. Homologue sequences were obtained by using hATG3 (NP_071933), hATG14L (NP_055739), hATG2A (NP_055919), hVPS34 (NP_002638) and hNUP133 (NP_060700) used as a reference sequence. We grouped the sequences by the family and phylum. The data set included 195 Chordata ATG3, 129 Arthropoda ATG3, 44 Nematoda ATG3, 177 Streptophyta ATG3, 419 Ascomycota ATG3, 157 Chordata ATG14, 366 Chordata ATG2, 219 Chordata VPS34, and 179 Chordata NUP133 and one yeast Spo20 protein sequences. The sequences were aligned on MEGA X software and the AH region was extracted. We calculated the amino acid composition and the physicochemical properties of the AHs based on HeliQuest algorithm (*38*). To analyze a large data set, we used a Python code "Hydrophobic Moment Calculator" (*52*) on GitHub with slight modifications. We computed the length, net charge, hydrophobicity, hydrophobic moment, the number of polar (S, T, N, H, Q, E, D, K and R), apolar (A, L, V, I, M, Y, W, F, P and C), charged (E, D, K and R), and bulky hydrophobic (F and W) residues, and the count of amino acids by residue type, for each AH in the data set. We normalized each feature by subtracting the mean and dividing by the standard deviation and analyzed the data with a custom-written Python code based on the Scikit-learn library (*53*). Subsequently, we conducted the principal component analysis (PCA) and restricted to the first 3 components, as they explain more than 50% of the data's variance. The importance of each feature within a principal component was evaluated according to the loading matrix.

Molecular modelling and system preparation

We obtained the human ATG3 and LC3B amino acid sequences from UniProt (entries Q9NT62 and Q9GZQ8, respectively (*54*)); of the latter, we selected residues 1-120. We ran two sets of atomistic molecular dynamics (MD) simulations. First, we simulated residues 1-24 of ATG3 (sequence MQNVINTVKGKALEVAEYLTPVLK) modeled as an alpha helix with UCSF Chimera (*55*). Second, we simulated the entire ATG3~LC3 conjugate. In the absence of an experimental structure, we modeled it with AlphaFold (*39, 56*). We entered the sequences and used the MMseqs2 homology search and pLDDT confidence measure to rank the models (*57*). We resolved 5 heterodimeric structures and selected the one with LC3 closest to the lipid bilayer.

We used CHARMM-GUI (*58, 59*) to model the lipid membrane and horizontally insert the N-terminus of ATG3 in the upper leaflet (Membrane Builder tool (*60*)) and to add the solvent and ions. In half of the systems, we point-mutated the ATG3 sequence. Finally, we created the topology and structure files for the MD simulations (*61*). The two versions of ATG3 are the wild-type (WT) and the 5W-mutated. In the latter, we turn Val4, Val8, Ala12, Val15, and

Ala16 into Tryptophan to increase the N-terminal helix's hydrophobicity.

We modeled a lipid bilayer with 55% 18:1/18:1-dioleoylphosphatidylethanolamine (DOPE), 30% 18:1/18:1-dioleoylphosphatidylcholine (DOPC), and 15% 18:0/20:4-1-stearoyl-2-arachidonoyl phosphatidylinositol (PI) with the CHARMMGUI membrane builder (*59, 60*). We placed the membrane leaflets horizontally in the simulation box. We inserted the ATG3's N-terminus parallel to the upper leaflet, with the helix's hydrophobic face pointing down. We capped the N and C-termini in all peptides to make them neutral. We used TIP3P water solvent and neutralized the system's net charge by adding 0.18 M of NaCl ions. We imposed periodic boundary conditions on the simulation boxes.

The systems in the first set have approx. 60k atoms and $8 \times 8 \times 9.8$ nm^3 boxes. Those in the second have 160k atoms and $10 \times 10 \times 15.8$ nm^3 boxes.

MD Simulations

We used the CHARMM36m force field (*61, 62*), and ran the simulations with GROMACS 2021.4 (*63-69*). We followed the energy minimization and 1 ns equilibration protocol provided by CHARMM-GUI. We launched NPT production runs with temperature T = 310 K (Nose-Hoover thermostat (*70*)), pressure P = 1 atm (semi-isotropic Parrinello-Rahman barostat (*71*)), and a 1.2 nm cutoff for both the Van der Walls and the Coulomb forces (particle mesh Ewald method (*72*)). We used a dt = 2 fs integration step and saved the configurations to GROMACS xtc trajectory files every 1 ns.

We modeled the thioester bond between Cys264 of Atg3 and Gly120 of LC3 as an "intramolecular interaction" in the GROMACS topology file. We applied a harmonic restraint between the Cysteine's sulfur and one of the Glycine's terminal oxygens after the original equilibration, with target distance d = 0.12 nm and force constant k = 6000 kJ $\cdot$ mol^{-1}nm^{-2}. Lower d and higher k resulted in simulation instabilities. We ran further 500 ps before starting the production run; the linked atoms ended up about 0.21 nm distant.

We describe the simulations in the following table:

Name	Description	Replica	Duration	Notes
wt ah	Wild-type residues 1-24 of Atg3 on the lipid membrane	run1	6.131 μs	
		run2	5.036 μs	
		run3	5.016 μs	
5w ah	5W-mutated residue 1-24 of Atg3 on the lipid membrane	run1	3.113 μs	

wt thioester	Wild-type Atg3-LC3 with the lipid membrane and the Cys-Gly thioester bond	run1	6.228 μs	Initiated from the Alphafold "up" configuration.
		run3	0.146 μs	
		run4	0.146 μs	
		run5	0.146 μs	
		run6	0.147 μs	
		run2	6.060 μs	Initiated from the "down" configuration of 5w, run1 at t = 4.7 μs, mutated back to WT.
		run7	0.437 μs	
		run8	0.435 μs	
		run9	0.297 μs	
		run10	0.299 μs	
5w thioester	5W-mutated Atg3-LC3 with the lipid membrane and the Cys-Gly thioester bond	run1	6.231 μs	Initiated from the 5W-mutated Alphafold "up" configuration.
		run3	0.146 μs	
		run4	0.146 μs	
		run5	0.146 μs	
		run6	0.148 μs	
		run2	4.843 μs	Initiated from the "down" configuration of 5w, run1 at t = 4.7 μs.
		run7	0.450 μs	
		run8	0.450 μs	
		run9	0.316 μs	
		run10	0.316 μs	
wt	Wild-type Atg3-LC3 with the lipid membrane without the Cys-Gly thioester bond	run1	12.282 μs	Initiated from the Alphafold "up" configuration.
		run2	8.108 μs	
		run3	7.963 μs	
		run4	7.462 μs	Initiated from the "down" configuration of 5w, run1 at t = 4.7 μs, mutated back to WT.
5w	5W-mutated Atg3-LC3 with the lipid membrane without the Cys-Gly thioester bond	run1	12.225 μs	Initiated from the 5W-mutated Alphafold "up" configuration.
		run2	9.129 μs	
		run3	9.042 μs	

Table 1: Simulated systems.

Replicas wt thioester run2, run7, run8, run9, and run10, 5w thioester run2, run7, run8, run9, and run10, and wt run4 were initiated from the 5w, run1 configuration at t = 4.7 μs. After careful inspection, we took such configuration as representative of the "down" conformation. In the WT simulations, we mutated it back to the original amino acid sequence with

CHARMM-GUI.

MD Trajectory analysis

We used the GROMACS trjconv tool to process the trajectories, and VMD 1.9 (*73*) for visual inspection and rendering. We kept the membrane leaflets horizontal and aligned the central axis of the AH's Cα to the $\hat{\mathbf{x}}$ direction once projected to the *XY* plane (N to C terminus). We performed numerical analysis in custom-written Python code based on the NumPy, SciPy, and MDTraj libraries (*74*).

We described the systems' dynamics with the following features:

α: the tilt angle of the central axis of the AH with respect to the horizontal plane;

r: the minimum distance between Atg3's TYR209 and the AH heavy atoms —it is a measure of the "compactness" of the complex;

We quantified the amino acid-lipid contacts by looking at the minimum distances d between the residue's heavy atoms and lipid phosphate heads. We considered the contact formed for $d < 0.45$. We computed the maximum persistence time for each contact as its most extended continuous series in a simulation. We enforced comparability by considering subtrajectories of equal length either in the "up" or "down" configurations (wt _thioesterrun1 and run2), first 6 μs).

Statistics and reproducibility

Differences were statistically analyzed by one-way ANOVA and Turkey multiple comparison test. Statistical analysis was carried out using GraphPad Prism 9 (GraphPad Software). All data are presented as the mean $\pm$ SEM. Reproducibility of all results reported here was confirmed.

Acknowledgements

21

Author Contributions

T.N. and S.A.T. conceived the project. T.N., R.C., and S.A.T. designed the research. T.N., G.L., and R.C. performed most experimental work and analyzed the data. T.N. and R.C. performed the AH data analysis. G.L. and R.C. designed, performed, and analyzed the MD simulation. T.N. performed the live imaging analysis. T.N., G.L., N.M., R.C., and S.A.T. wrote the manuscript with input from all authors.

Conflict of Interest

The authors declare no competing interests.

References

1. N. Mizushima, T. Yoshimori, Y. Ohsumi, The role of Atg proteins in autophagosome formation. *Annual review of cell and developmental biology* **27**, 107-132 (2011).

2. H. Nakatogawa, Mechanisms governing autophagosome biogenesis. *Nature reviews. Molecular cell biology* **21**, 439-458 (2020).

3. C. Chang, L. E. Jensen, J. H. Hurley, Autophagosome biogenesis comes out of the black box. *Nature cell biology* **23**, 450-456 (2021).

4. E. Adriaenssens, L. Ferrari, S. Martens, Orchestration of selective autophagy by cargo receptors. *Current biology : CB* **32**, R1357-R1371 (2022).

5. T. J. Melia, A. H. Lystad, A. Simonsen, Autophagosome biogenesis: From membrane growth to closure. *The Journal of cell biology* **219**,   (2020).

6. N. Nguyen, V. Shteyn, T. J. Melia, Sensing Membrane Curvature in Macroautophagy. *Journal of molecular biology* **429**, 457-472 (2017).

7. T. Nishimura, S. A. Tooze, Emerging roles of ATG proteins and membrane lipids in autophagosome formation. *Cell Discov* **6**, 32 (2020).

8. A. R. van Vliet, G. N. Chiduza, S. L. Maslen, V. E. Pye, D. Joshi, S. De Tito, H. B. J. Jefferies, E. Christodoulou, C. Roustan, E. Punch, J. H. Hervas, N. O'Reilly, J. M. Skehel, P. Cherepanov, S. A. Tooze, ATG9A and ATG2A form a heteromeric complex essential for autophagosome formation. *Molecular cell* **82**, 4324-4339 e4328 (2022).

9. N. N. Noda, Atg2 and Atg9: Intermembrane and interleaflet lipid transporters driving autophagy. *Biochimica et biophysica acta. Molecular and cell biology of lipids* **1866**, 158956 (2021).

10. K. M. Reinisch, X. W. Chen, T. J. Melia, "VTT"-domain proteins VMP1 and TMEM41B function in lipid homeostasis globally and locally as ER scramblases. *Contact (Thousand Oaks)* **4**,   (2021).

11. H. Nakatogawa, Y. Ichimura, Y. Ohsumi, Atg8, a ubiquitin-like protein required for autophagosome formation, mediates membrane tethering and hemifusion. *Cell* **130**, 165-178 (2007).

12. T. Maruyama, J. M. Alam, T. Fukuda, S. Kageyama, H. Kirisako, Y. Ishii, I. Shimada, Y. Ohsumi, M. Komatsu, T. Kanki, H. Nakatogawa, N. N. Noda, Membrane perturbation by lipidated Atg8 underlies autophagosome biogenesis. *Nature structural & molecular biology* **28**, 583-593 (2021).

13. Y. Sakai, I. Koyama-Honda, M. Tachikawa, R. L. Knorr, N. Mizushima, Modeling Membrane Morphological Change during Autophagosome Formation. *iScience* **23**, 101466 (2020).

14. W. Zhang, T. Nishimura, D. Gahlot, C. Saito, C. Davis, H. B. J. Jefferies, A. Schreiber, L.

Thukral, S. A. Tooze, Cis-membrane association of human ATG8 proteins N-terminus mediates autophagy. *bioRxiv*, 2022.2006.2010.495627 (2022).

15. I. Koyama-Honda, E. Itakura, T. K. Fujiwara, N. Mizushima, Temporal analysis of recruitment of mammalian ATG proteins to the autophagosome formation site. *Autophagy* **9**, 1491-1499 (2013).

16. E. Karanasios, S. A. Walker, H. Okkenhaug, M. Manifava, E. Hummel, H. Zimmermann, Q. Ahmed, M. C. Domart, L. Collinson, N. T. Ktistakis, Autophagy initiation by ULK complex assembly on ER tubulovesicular regions marked by ATG9 vesicles. *Nature communications* **7**, 12420 (2016).

17. M. Gimenez-Andres, A. Copic, B. Antonny, The Many Faces of Amphipathic Helices. *Biomolecules* **8**, (2018).

18. N. Tamura, T. Nishimura, Y. Sakamaki, I. Koyama-Honda, H. Yamamoto, N. Mizushima, Differential requirement for ATG2A domains for localization to autophagic membranes and lipid droplets. *FEBS letters* **591**, 3819-3830 (2017).

19. A. H. Lystad, S. R. Carlsson, L. R. de la Ballina, K. J. Kauffman, S. Nag, T. Yoshimori, T. J. Melia, A. Simonsen, Distinct functions of ATG16L1 isoforms in membrane binding and LC3B lipidation in autophagy-related processes. *Nature cell biology* **21**, 372-383 (2019).

20. Y. Ohashi, S. Tremel, G. R. Masson, L. McGinney, J. Boulanger, K. Rostislavleva, C. M. Johnson, I. Niewczas, J. Clark, R. L. Williams, Membrane characteristics tune activities of endosomal and autophagic human VPS34 complexes. *eLife* **9**, (2020).

21. N. Gopaldass, B. Fauvet, H. Lashuel, A. Roux, A. Mayer, Membrane scission driven by the PROPPIN Atg18. *The EMBO journal* **36**, 3274-3291 (2017).

22. S. Nath, J. Dancourt, V. Shteyn, G. Puente, W. M. Fong, S. Nag, J. Bewersdorf, A. Yamamoto, B. Antonny, T. J. Melia, Lipidation of the LC3/GABARAP family of autophagy proteins relies on a membrane-curvature-sensing domain in Atg3. *Nature cell biology* **16**, 415-424 (2014).

23. M. Hamasaki, N. Furuta, A. Matsuda, A. Nezu, A. Yamamoto, N. Fujita, H. Oomori, T. Noda, T. Haraguchi, Y. Hiraoka, A. Amano, T. Yoshimori, Autophagosomes form at ER-mitochondria contact sites. *Nature* **495**, 389-393 (2013).

24. T. Nishimura, N. Tamura, N. Kono, Y. Shimanaka, H. Arai, H. Yamamoto, N. Mizushima, Autophagosome formation is initiated at phosphatidylinositol synthase-enriched ER subdomains. *The EMBO journal* **36**, 1719-1735 (2017).

25. K. Suzuki, M. Akioka, C. Kondo-Kakuta, H. Yamamoto, Y. Ohsumi, Fine mapping of autophagy-related proteins during autophagosome formation in Saccharomyces cerevisiae. *Journal of cell science* **126**, 2534-2544 (2013).

26. M. Graef, J. R. Friedman, C. Graham, M. Babu, J. Nunnari, ER exit sites are physical and

functional core autophagosome biogenesis components. *Molecular biology of the cell* **24**, 2918-2931 (2013).

27. R. Le Bars, J. Marion, R. Le Borgne, B. Satiat-Jeunemaitre, M. W. Bianchi, ATG5 defines a phagophore domain connected to the endoplasmic reticulum during autophagosome formation in plants. *Nature communications* **5**, 4121 (2014).

28. T. Hanada, Y. Satomi, T. Takao, Y. Ohsumi, The amino-terminal region of Atg3 is essential for association with phosphatidylethanolamine in Atg8 lipidation. *FEBS letters* **583**, 1078-1083 (2009).

29. J. H. Hervas, A. Landajuela, Z. Anton, A. V. Shnyrova, F. M. Goni, A. Alonso, Human ATG3 binding to lipid bilayers: role of lipid geometry, and electric charge. *Scientific reports* **7**, 15614 (2017).

30. M. D. Stewart, T. Ritterhoff, R. E. Klevit, P. S. Brzovic, E2 enzymes: more than just middle men. *Cell research* **26**, 423-440 (2016).

31. L. Cappadocia, C. D. Lima, Ubiquitin-like Protein Conjugation: Structures, Chemistry, and Mechanism. *Chem Rev* **118**, 889-918 (2018).

32. Y. Ye, E. R. Tyndall, V. Bui, Z. Tang, Y. Shen, X. Jiang, J. M. Flanagan, H. G. Wang, F. Tian, An N-terminal conserved region in human Atg3 couples membrane curvature sensitivity to conjugase activity during autophagy. *Nature communications* **12**, 374 (2021).

33. L. E. Jensen, S. Rao, M. Schuschnig, A. K. Cada, S. Martens, G. Hummer, J. H. Hurley, Membrane curvature sensing and stabilization by the autophagic LC3 lipidation machinery. *Science advances* **8**, eadd1436 (2022).

34. S. Wang, Y. Li, C. Ma, Atg3 promotes Atg8 lipidation via altering lipid diffusion and rearrangement. *Protein Sci* **29**, 1511-1523 (2020).

35. G. Drin, J. F. Casella, R. Gautier, T. Boehmer, T. U. Schwartz, B. Antonny, A general amphipathic alpha-helical motif for sensing membrane curvature. *Nature structural & molecular biology* **14**, 138-146 (2007).

36. H. Horchani, M. de Saint-Jean, H. Barelli, B. Antonny, Interaction of the Spo20 membrane-sensor motif with phosphatidic acid and other anionic lipids, and influence of the membrane environment. *PloS one* **9**, e113484 (2014).

37. M. Sakoh-Nakatogawa, H. Kirisako, H. Nakatogawa, Y. Ohsumi, Localization of Atg3 to autophagy-related membranes and its enhancement by the Atg8-family interacting motif to promote expansion of the membranes. *FEBS letters* **589**, 744-749 (2015).

38. R. Gautier, D. Douguet, B. Antonny, G. Drin, HELIQUEST: a web server to screen sequences with specific alpha-helical properties. *Bioinformatics* **24**, 2101-2102 (2008).

39. J. Jumper, R. Evans, A. Pritzel, T. Green, M. Figurnov, O. Ronneberger, K. Tunyasuvunakool, R. Bates, A. Zidek, A. Potapenko, A. Bridgland, C. Meyer, S. A. A. Kohl,

A. J. Ballard, A. Cowie, B. Romera-Paredes, S. Nikolov, R. Jain, J. Adler, T. Back, S. Petersen, D. Reiman, E. Clancy, M. Zielinski, M. Steinegger, M. Pacholska, T. Berghammer, S. Bodenstein, D. Silver, O. Vinyals, A. W. Senior, K. Kavukcuoglu, P. Kohli, D. Hassabis, Highly accurate protein structure prediction with AlphaFold. *Nature* **596**, 583-589 (2021).

40.   J. Farnung, M. Muhar, J. R. Liang, K. A. Tolmachova, R. M. Benoit, J. E. Corn, J. W. Bode, Human ATG3 contains a non-canonical LIR motif crucial for its enzymatic activity in autophagy. *bioRxiv*, 2022.2008.2002.502437 (2022).

41.   M. Sakoh-Nakatogawa, K. Matoba, E. Asai, H. Kirisako, J. Ishii, N. N. Noda, F. Inagaki, H. Nakatogawa, Y. Ohsumi, Atg12-Atg5 conjugate enhances E2 activity of Atg3 by rearranging its catalytic site. *Nature structural & molecular biology* **20**, 433-439 (2013).

42.   Y. Zheng, Y. Qiu, C. R. R. Grace, X. Liu, D. J. Klionsky, B. A. Schulman, A switch element in the autophagy E2 Atg3 mediates allosteric regulation across the lipidation cascade. *Nature communications* **10**, 3600 (2019).

43.   Z. Metlagel, C. Otomo, G. Takaesu, T. Otomo, Structural basis of ATG3 recognition by the autophagic ubiquitin-like protein ATG12. *Proceedings of the National Academy of Sciences of the United States of America* **110**, 18844-18849 (2013).

44.   N. N. Noda, Y. Fujioka, T. Hanada, Y. Ohsumi, F. Inagaki, Structure of the Atg12-Atg5 conjugate reveals a platform for stimulating Atg8-PE conjugation. *EMBO reports* **14**, 206-211 (2013).

45.   J. I. Sakamaki, K. L. Ode, Y. Kurikawa, H. R. Ueda, H. Yamamoto, N. Mizushima, Ubiquitination of phosphatidylethanolamine in organellar membranes. *Molecular cell* **82**, 3677-3692 e3611 (2022).

46.   H. F. Hofbauer, M. Gecht, S. C. Fischer, A. Seybert, A. S. Frangakis, E. H. K. Stelzer, R. Covino, G. Hummer, R. Ernst, The molecular recognition of phosphatidic acid by an amphipathic helix in Opi1. *The Journal of cell biology* **217**, 3109-3126 (2018).

47.   R. Covino, G. Hummer, R. Ernst, Integrated Functions of Membrane Property Sensors and a Hidden Side of the Unfolded Protein Response. *Molecular cell* **71**, 458-467 (2018).

48.   I. Levental, E. Lyman, Regulation of membrane protein structure and function by their lipid nano-environment. *Nature reviews. Molecular cell biology* **24**, 107-122 (2023).

49.   K. Motohashi, A simple and efficient seamless DNA cloning method using SLiCE from Escherichia coli laboratory strains and its application to SLiP site-directed mutagenesis. *Bmc Biotechnol* **15**,   (2015).

50.   N. Hosokawa, Y. Hara, N. Mizushima, Generation of cell lines with tetracycline-regulated autophagy and a role for autophagy in controlling cell size. *FEBS letters* **580**, 2623-2629 (2006).

51.   Y. S. Sou, S. Waguri, J. Iwata, T. Ueno, T. Fujimura, T. Hara, N. Sawada, A. Yamada, N. Mizushima, Y. Uchiyama, E. Kominami, K. Tanaka, M. Komatsu, The Atg8 conjugation system is indispensable for proper development of autophagic isolation membranes in mice. *Molecular biology of the cell* **19**, 4762-4775 (2008).

52.   https://github.com/JoaoRodrigues/hydrophobic_moment.

53.   F. Pedregosa, G. Varoquaux, A. Gramfort, V. Michel, B. Thirion, O. Grisel, M. Blondel, P. Prettenhofer, R. Weiss, V. Dubourg, J. Vanderplas, A. Passos, D. Cournapeau, M. Brucher, M. Perrot, E. Duchesnay, Scikit-learn: Machine Learning in Python. *J Mach Learn Res* **12**, 2825-2830 (2011).

54.   C. UniProt, UniProt: a hub for protein information. *Nucleic acids research* **43**, D204-212 (2015).

55.   Z. Yang, K. Lasker, D. Schneidman-Duhovny, B. Webb, C. C. Huang, E. F. Pettersen, T. D. Goddard, E. C. Meng, A. Sali, T. E. Ferrin, UCSF Chimera, MODELLER, and IMP: an integrated modeling system. *Journal of structural biology* **179**, 269-278 (2012).

56.   R. Evans, M. O'Neill, A. Pritzel, N. Antropova, A. Senior, T. Green, A. Žídek, R. Bates, S. Blackwell, J. Yim, O. Ronneberger, S. Bodenstein, M. Zielinski, A. Bridgland, A. Potapenko, A. Cowie, K. Tunyasuvunakool, R. Jain, E. Clancy, P. Kohli, J. Jumper, D. Hassabis, Protein complex prediction with AlphaFold-Multimer. *bioRxiv*, 2021.2010.2004.463034 (2022).

57.   M. Mirdita, K. Schutze, Y. Moriwaki, L. Heo, S. Ovchinnikov, M. Steinegger, ColabFold: making protein folding accessible to all. *Nature methods* **19**, 679-682 (2022).

58.   S. Jo, T. Kim, V. G. Iyer, W. Im, CHARMM-GUI: a web-based graphical user interface for CHARMM. *Journal of computational chemistry* **29**, 1859-1865 (2008).

59.   S. Jo, J. B. Lim, J. B. Klauda, W. Im, CHARMM-GUI Membrane Builder for mixed bilayers and its application to yeast membranes. *Biophysical journal* **97**, 50-58 (2009).

60.   E. L. Wu, X. Cheng, S. Jo, H. Rui, K. C. Song, E. M. Davila-Contreras, Y. Qi, J. Lee, V. Monje-Galvan, R. M. Venable, J. B. Klauda, W. Im, CHARMM-GUI Membrane Builder toward realistic biological membrane simulations. *Journal of computational chemistry* **35**, 1997-2004 (2014).

61.   J. Lee, X. Cheng, J. M. Swails, M. S. Yeom, P. K. Eastman, J. A. Lemkul, S. Wei, J. Buckner, J. C. Jeong, Y. Qi, S. Jo, V. S. Pande, D. A. Case, C. L. Brooks, 3rd, A. D. MacKerell, Jr., J. B. Klauda, W. Im, CHARMM-GUI Input Generator for NAMD, GROMACS, AMBER, OpenMM, and CHARMM/OpenMM Simulations Using the CHARMM36 Additive Force Field. *Journal of chemical theory and computation* **12**, 405-413 (2016).

62.   J. Huang, S. Rauscher, G. Nawrocki, T. Ran, M. Feig, B. L. de Groot, H. Grubmuller, A.

D. MacKerell, Jr., CHARMM36m: an improved force field for folded and intrinsically disordered proteins. *Nature methods* **14**, 71-73 (2017).

63. S. Pall, M. J. Abraham, C. Kutzner, B. Hess, E. Lindahl, Tackling Exascale Software Challenges in Molecular Dynamics Simulations with GROMACS. *Lect Notes Comput Sc* **8759**, 3-27 (2015).

64. S. Pronk, S. Pall, R. Schulz, P. Larsson, P. Bjelkmar, R. Apostolov, M. R. Shirts, J. C. Smith, P. M. Kasson, D. van der Spoel, B. Hess, E. Lindahl, GROMACS 4.5: a high-throughput and highly parallel open source molecular simulation toolkit. *Bioinformatics* **29**, 845-854 (2013).

65. B. Hess, C. Kutzner, D. van der Spoel, E. Lindahl, GROMACS 4: Algorithms for highly efficient, load-balanced, and scalable molecular simulation. *Journal of chemical theory and computation* **4**, 435-447 (2008).

66. D. Van der Spoel, E. Lindahl, B. Hess, G. Groenhof, A. E. Mark, H. J. C. Berendsen, GROMACS: Fast, flexible, and free. *Journal of computational chemistry* **26**, 1701-1718 (2005).

67. H. J. C. Berendsen, D. Vanderspoel, R. Vandrunen, Gromacs - a Message-Passing Parallel Molecular-Dynamics Implementation. *Comput Phys Commun* **91**, 43-56 (1995).

68. E. Lindahl, M. J. Abraham, B. Hess, V. D. Spoel. (2021).

69. M. J. Abraham, T. Murtola, R. Schulz, S. Páll, J. C. Smith, B. Hessa, E. Lindahl, GROMACS: High performance molecular simulations through multi-level parallelism from laptops to supercomputers. *SoftwareX* **1-2**, 19-25 (2015).

70. D. J. Evans, B. L. Holian, The Nose-Hoover Thermostat. *Journal of Chemical Physics* **83**, 4069-4074 (1985).

71. D. Quigley, M. I. J. Probert, Langevin dynamics in constant pressure extended systems. *Journal of Chemical Physics* **120**, 11432-11441 (2004).

72. U. Essmann, L. Perera, M. L. Berkowitz, T. Darden, H. Lee, L. G. Pedersen, A Smooth Particle Mesh Ewald Method. *Journal of Chemical Physics* **103**, 8577-8593 (1995).

73. W. Humphrey, A. Dalke, K. Schulten, VMD: Visual molecular dynamics. *J Mol Graph Model* **14**, 33-38 (1996).

74. R. T. McGibbon, K. A. Beauchamp, M. P. Harrigan, C. Klein, J. M. Swails, C. X. Hernandez, C. R. Schwantes, L. P. Wang, T. J. Lane, V. S. Pande, MDTraj: A Modern Open Library for the Analysis of Molecular Dynamics Trajectories. *Biophysical journal* **109**, 1528-1532 (2015).
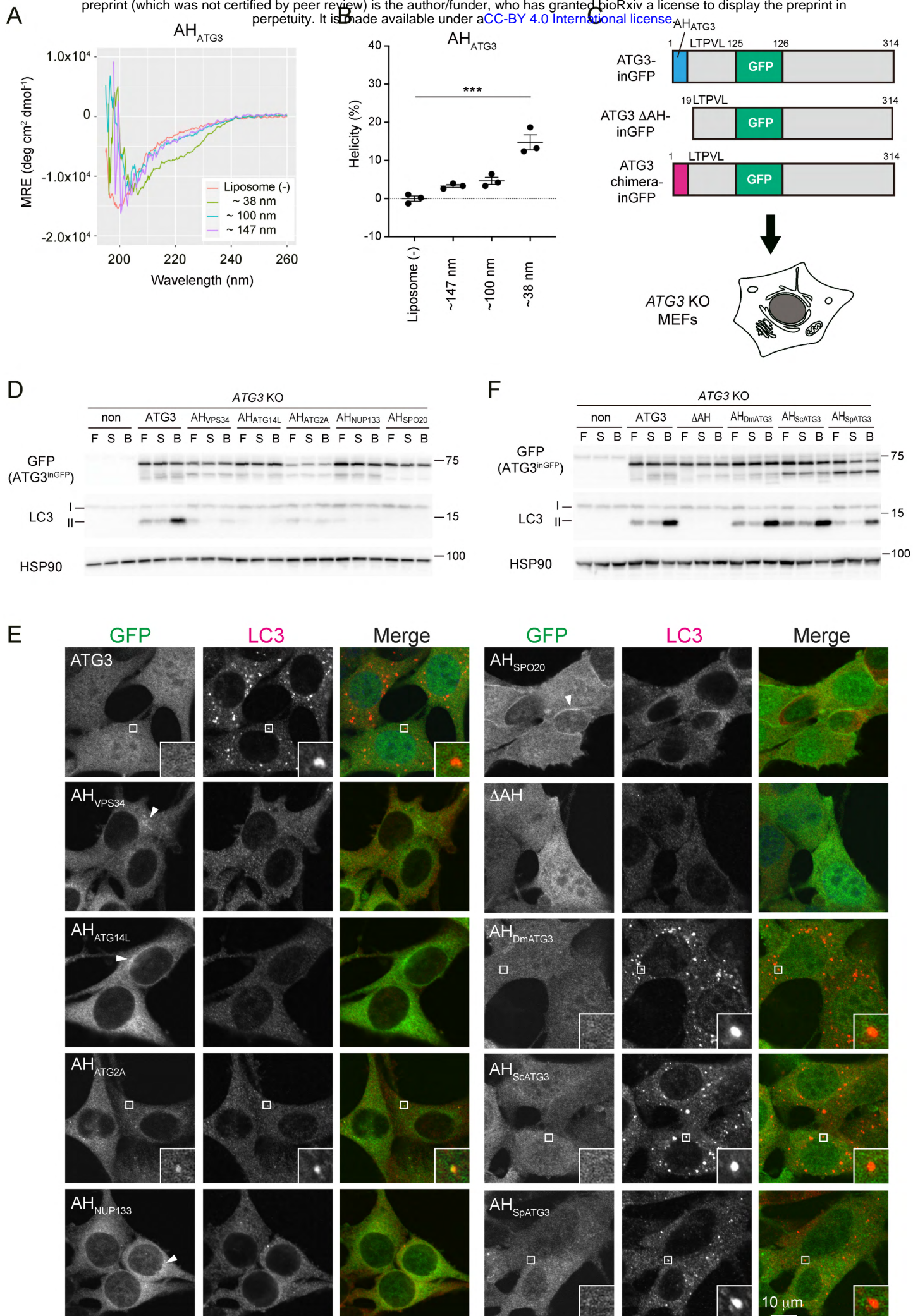
Figure 1

Figure 1. AH$_{ATG3}$ cannot be substituted for by unrelated AHs in human ATG3 protein.
(**A**) Far-UV CD spectra of AH$_{ATG3}$ peptide (75 µM) in the absence or presence of DOPC/DOPE (70/30) liposomes (6 mM). A peptide corresponding to the N-terminal ATG3 (1-22 aa) sequence and containing an additional C-terminal WK residues was used to facilitate titration by UV spectroscopy. The diameter of sonicated liposomes, liposomes extruded through 0.1 µm or 0.2 µm filters were 38 nm, 100 nm, and 147 nm, respectively. MRE, mean residue ellipticity. (**B**) Helicity at 222 nm as determined from the spectra shown in panel **A**. Data represent the mean ± SEM of three independent experiments. (**C**) An experimental scheme of ATG3 rescue assay using ATG3 chimeras. *ATG3 KO* MEFs expressing ATG3 WT, ATG3 ΔAH deletion mutant or ATG3 chimera were used to analyze LC3 lipidation and LC3 puncta formation. The domain organization of ATG3-inGFP is shown: A GFP tag is inserted into the region after E125 residue. P21 and L23 in the conserved region following AH$_{ATG3}$ are coded in all ATG3 constructs. (**D, F**) LC3 flux assay. The indicated cells were starved for 6h with (B) or without 100 nM Bafilomycin A$_1$ (S) or cultured in full media (F). Cell lysates were analyzed by immunoblotting using the indicated antibodies. (**E**) LC3 puncta formation. The cells were starved for 1 h, fixed and stained with anti-LC3 antibody. The specimens were analyzed by FV3000 confocal microscope. Arrowheads indicate the membrane localization of ATG3 chimeras. Scale bar, 10 µm. Differences were statistically analyzed by one-way ANOVA and Turkey multiple comparison test. ***$P < 0.001$.

See also Figure S1.
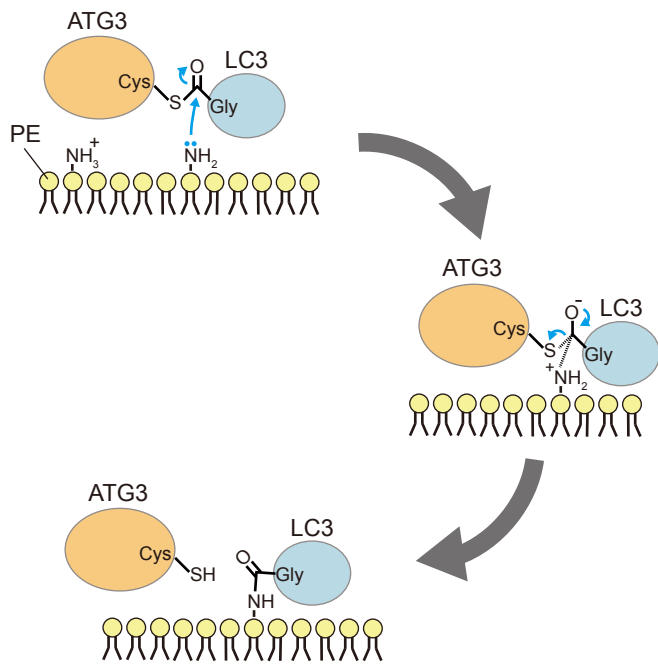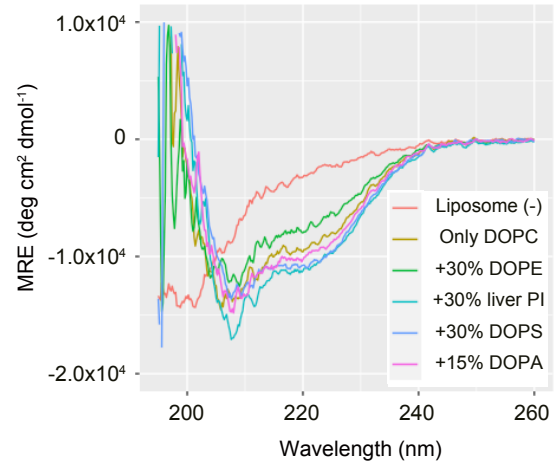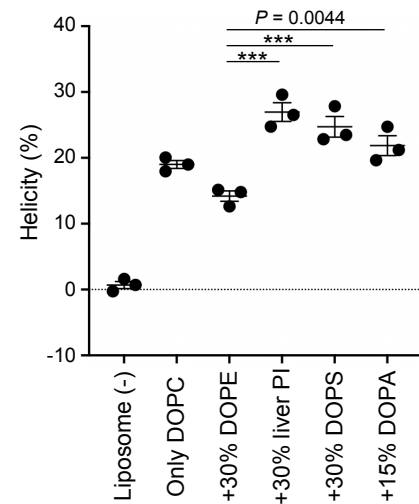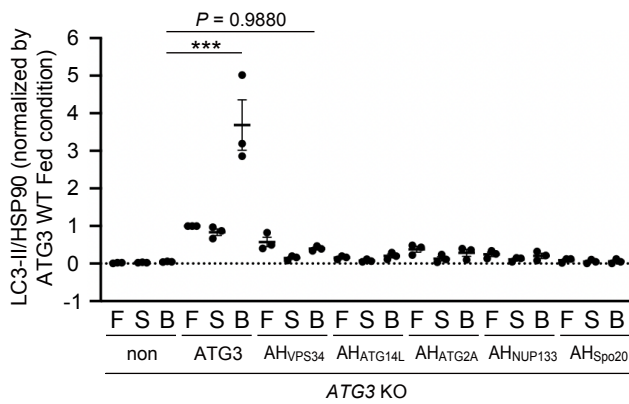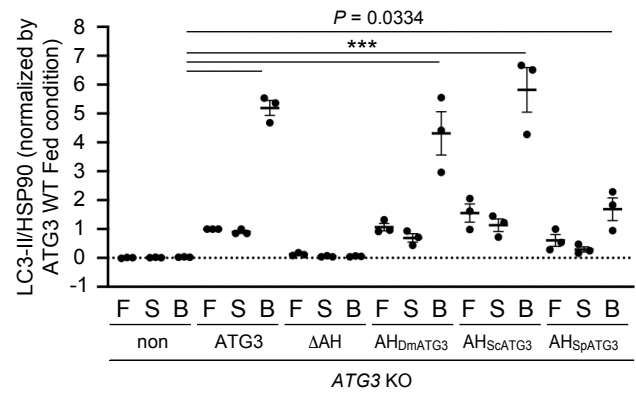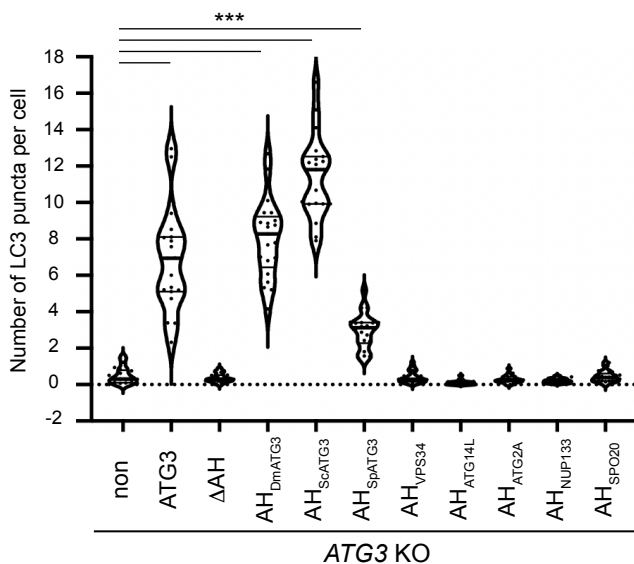
Figure S1

Figure S1 related to Figure 1. ATG3-dependent LC3 conjugation reaction and quantification results of ATG3 rescue assay.

(**A**) The chemical mechanism of LC3–PE conjugation catalyzed by ATG3. (top) An ATG3~LC3 conjugate interacts with membranes. The primary amine of PE head group, which is mostly in the protonated state at physiological pH, becomes deprotonated for nucleophilic attack on the thioester bond linking ATG3 and LC3. (middle) After nucleophilic attack, the negatively charged thioester oxygen atom is formed, and it is expected to be stabilized by surrounding residues. (bottom) Simultaneously, ATG3 is dissociated from the intermediate structure and leaves the membranes, which results in the formation of an amide bond between LC3 and PE. (**B**) Far-UV CD spectra of AH$_{ATG3}$ peptide (75 µM) in the absence or presence of sonicated liposomes (6 mM) containing increasing mol% of either DOPE, liver PI, DOPS or DOPA. The remaining lipids in the liposome were DOPC (the concentration of which varied from 70 mol% to 100 mol% depending on the concentration of another lipid). MRE, mean residue ellipticity. (**C**) Helicity at 222 nm as determined from the spectra shown in Fig. S1B. (**D**) Band intensity quantification of LC3-II shown in Fig. 1D. All data were normalized with those of HSP90. (**E**) Quantification of the number of LC3 puncta shown in Fig. 1E. The thick and thin lines in the violin plot represent the medians and quartiles, respectively. The average number of LC3 puncta per cell was counted from randomly selected areas (n≧19). (**F**) Band intensity quantification of LC3-II shown in Fig. 1F. All data were normalized with those of HSP90. Data represent the mean ± SEM of three independent experiments (**C, D, F**). Differences were statistically analyzed by one-way ANOVA and Turkey multiple comparison test. ***$P < 0.001$.
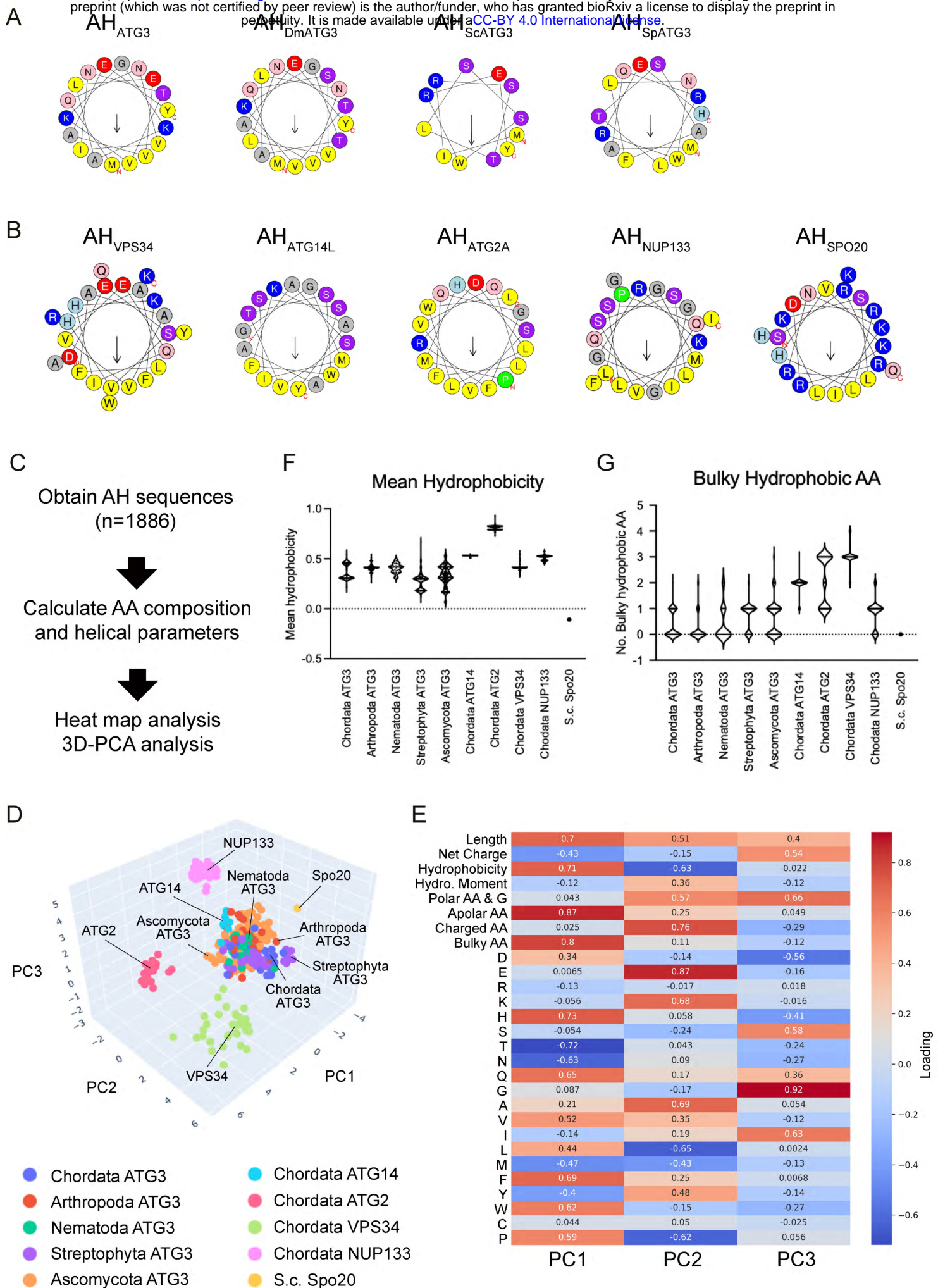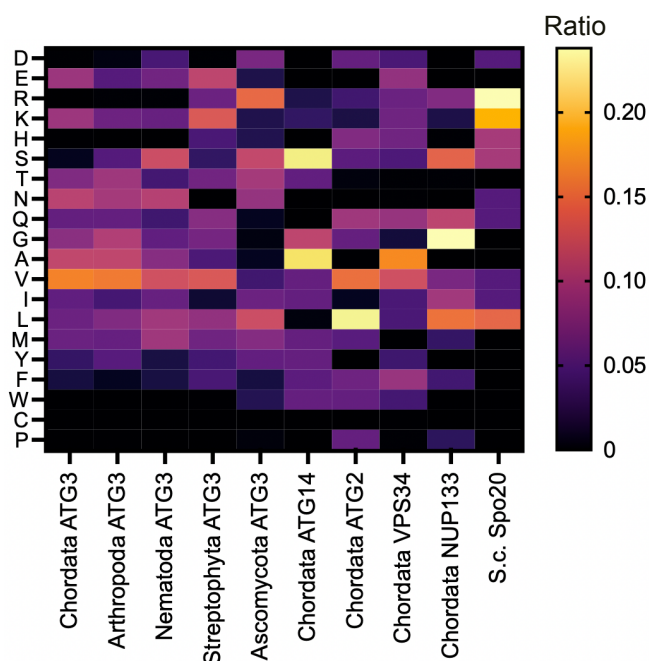
Figure 2

Figure 2. Characterization of conserved AH_{ATG3} features by unsupervised machine learning.

(**A, B**) The amphipathic properties of AHs used in the ATG3 rescue assay. Helical wheel representations of AHs derived from ATG3 proteins (**A**) and other unrelated proteins (**B**) were generated in HeliQuest. Hydrophobic residues are shown in yellow, arginine and lysine in dark blue, histidine in light blue, serine and threonine in purple, glutamine and asparagine in pink, proline in green, glutamate and aspartate in red and glycine and alanine in gray. Arrows in helical wheels correspond to the hydrophobic moment. (**C**) Flow chart of AH data analysis. (**D**) Three-dimensional principal component analysis (PCA) of amino acid composition and helical parameter data set. AHs derived from ATG3 proteins were categorized into five groups by phylum: Chordata, Arthropoda, Nematoda, Streptophyta and Ascomycota. Each of the groups is represented by the indicated color. (**E**) PCA Loading matrix. The number of polar residues (Polar AA: S, T, N, H, Q, E, D, K and R), apolar residues (Apolar AA: A, L, V, I, M, Y, W, F, P and C), charged residues (Charged AA: E, D, K and R), and bulky hydrophobic residues (Bulky AA: F and W) were used in the PCA analysis. (**F, G**) Mean hydrophobicity (**F**) and the number of bulky hydrophobic residues (**G**) of AHs. The thick and thin lines in the violin plot represent the medians and quartiles of each group, respectively.
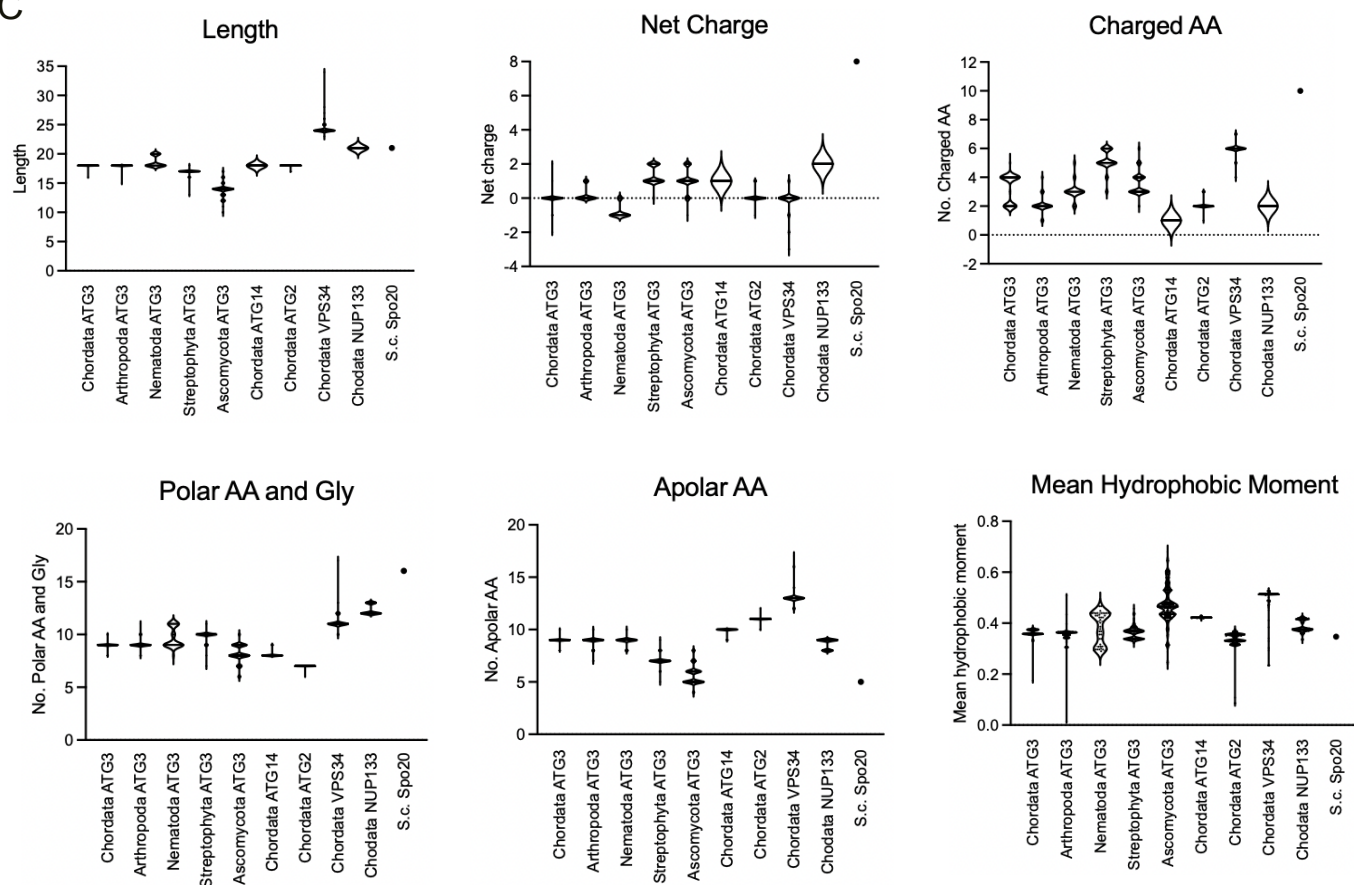
See also Figure S2.
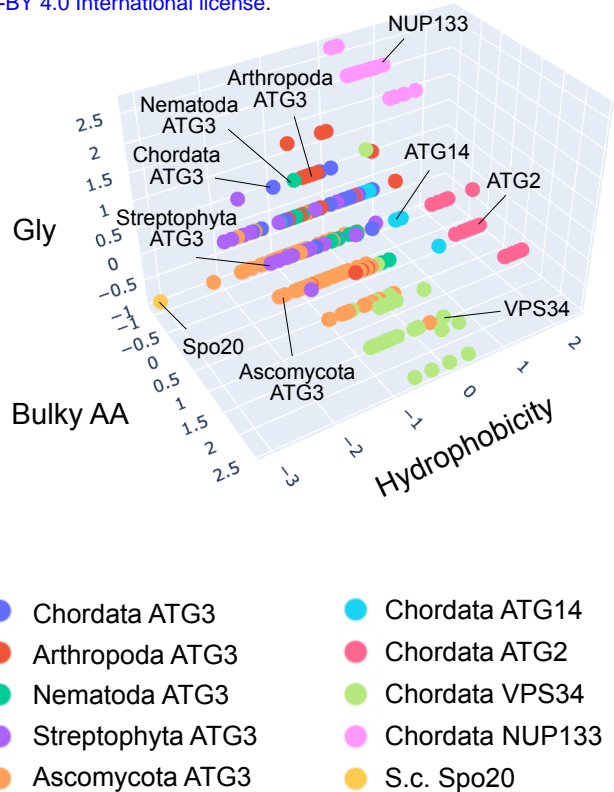
Figure S2

Figure S2 related to Figure 2. Helical parameters of AHs analyzed in this study.

(**A**) Heatmap of amino acid composition of AHs. AHs derived from ATG3 proteins were categorized into five groups by phylum: Chordata, Arthropoda, Nematoda, Streptophyta and Ascomycota. (**B**) A 3D-plot of the number of bulky residues, glycine residues and mean hydrophobicity of AHs analyzed in this study. Each of the groups is represented by the indicated colors. (**C**) Length, net charge, the number of charged residue (Charged AA), the number of polar residue and glycine residue (Polar AA and Gly), the number of apolar residue (Apolar AA) and mean hydrophobic moment are shown. The thick and thin lines in the violin plot represent the medians and quartiles of each group, respectively.
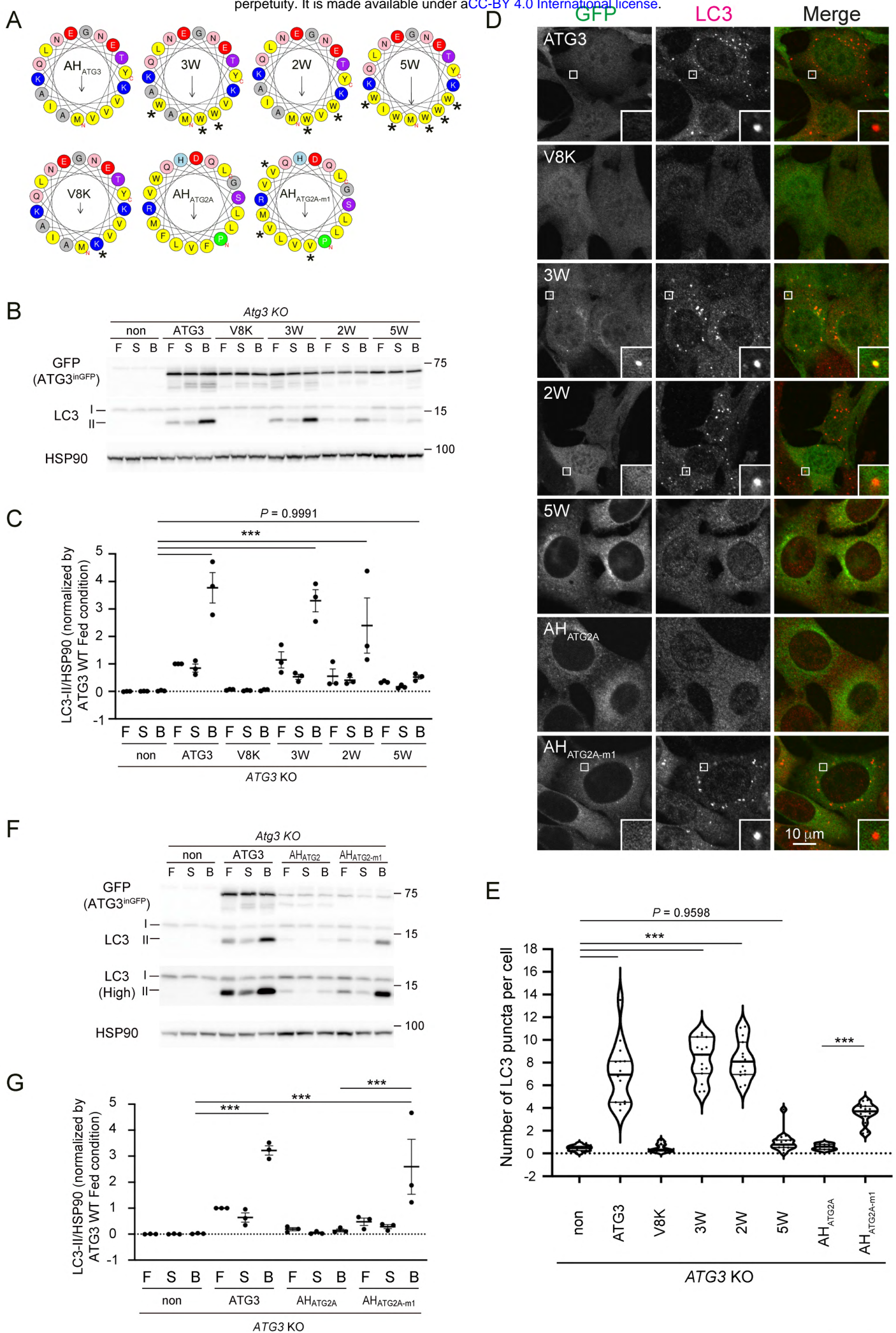
Figure 3

Figure 3. Low hydrophobicity and less bulky features are crucial for AH$_{ATG3}$ to be functional for LC3 lipidation.

(**A**) Helical wheel representations of higher bulky-hydrophobic AH$_{ATG3}$ and less bulky-hydrophobic AH$_{ATG2A}$ mutants. V8K mutation destroys the amphipathic character of AH$_{ATG3}$. Asterisks indicate the position of mutations. (**B**) LC3 flux assay of *ATG3* KO cells expressing ATG3 WT or the indicated ATG3 mutants. The cells were starved for 6h with (B) or without 100 nM Bafilomycin A$_1$ (S) or cultured in full media (F). Cell lysates were analyzed by immunoblotting using the indicated antibodies. (**C**) Band intensity quantification of LC3-II. All data were normalized with those of HSP90. Data represent the mean ± SEM of three independent experiments. (**D**) LC3 puncta formation. The cells were starved for 1 h, fixed and stained with anti-LC3 antibody. The specimens were analyzed by FV3000 confocal microscope. Scale bar, 10 μm. (**E**) Quantification of the number of LC3 puncta. The thick and thin lines in the violin plot represent the medians and quartiles, respectively. The average number of LC3 puncta per cell was counted from randomly selected areas (n≧14). (**F**) LC3 flux assay of *ATG3* KO cells expressing ATG3 WT or the indicated ATG3 chimeras. Note that ATG3 chimera carrying less bulky-hydrophobic mutant ATG2A-m1 showed the partial restoration of LC3 lipidation. (**G**) Band intensity quantification of LC3-II. All data were normalized with those of HSP90. Data represent the mean ± SEM of three independent experiments. Differences were statistically analyzed by one-way ANOVA and Turkey multiple comparison test. ***$P < 0.001$.
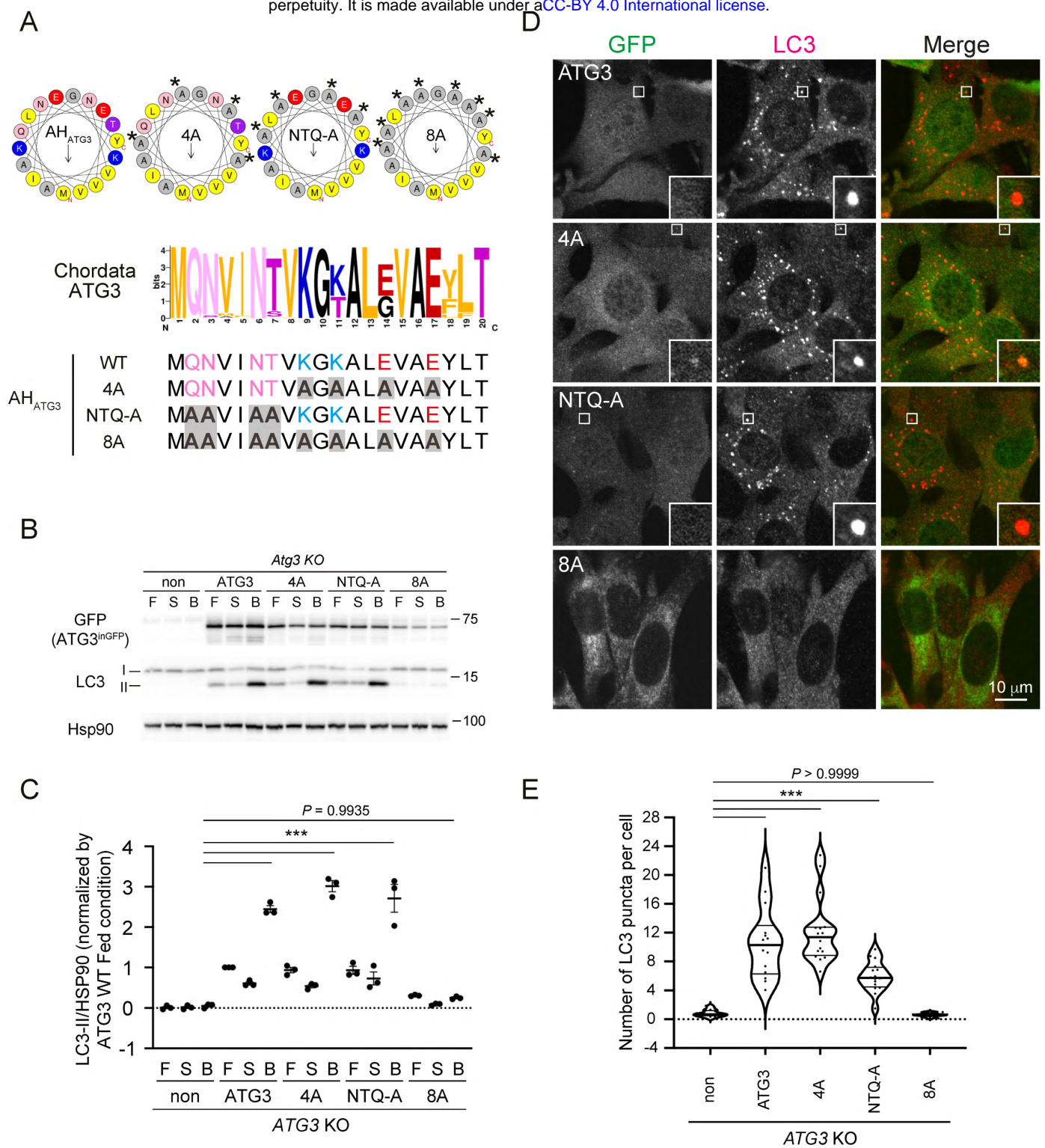
See also Figure S3.

A

B

C

D

E

Figure S3

Figure S3 related to Figure 3. Requirement of polar residues in the hydrophilic face of AH$_{ATG3}$.

(**A**) (top) Helical wheel representations of AH$_{ATG3}$ mutants containing mutations in its hydrophilic face. Asterisks indicate the position of mutations. (middle) WebLogo to represent amino acid sequence conservation among AHs of Chordata species' ATG3 proteins. (bottom) Multiple sequence alignment of AH regions of ATG3 WT and mutants. The positions of mutation are marked by gray shadow. (**B**) LC3 flux assay of *ATG3* KO cells expressing ATG3 WT or the indicated ATG3 mutants. The cells were starved for 6h with (B) or without 100 nM Bafilomycin A$_1$ (S) or cultured in full media (F). Cell lysates were analyzed by immunoblotting using the indicated antibodies. (**C**) Band intensity quantification of LC3-II shown in Fig. S3B. All data were normalized with those of HSP90. Data represent the mean ± SEM of three independent experiments. (**D**) LC3 puncta formation. The cells were starved for 1 h, fixed and stained with anti-LC3 antibody. The specimens were analyzed by FV3000 confocal microscope. Scale bar, 10 μm. (**E**) Quantification of the number of LC3 puncta. The thick and thin lines in the violin plot represent the medians and quartiles, respectively. The average number of LC3 puncta per cell was counted from randomly selected areas (n≧14). Differences were statistically analyzed by one-way ANOVA and Turkey multiple comparison test. ***$P < 0.001$.
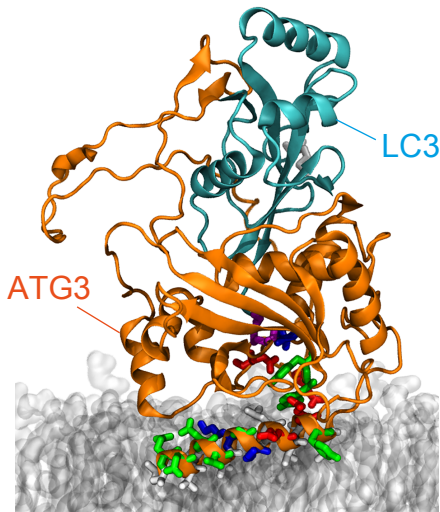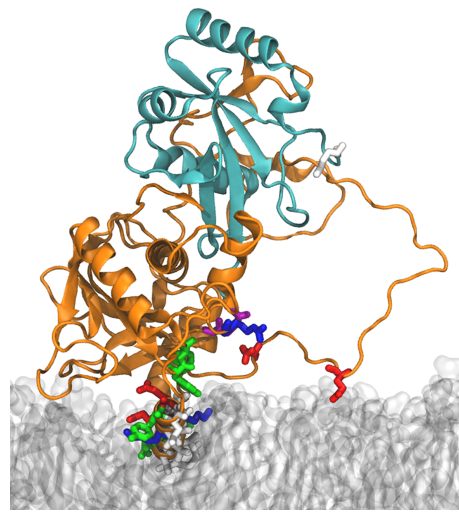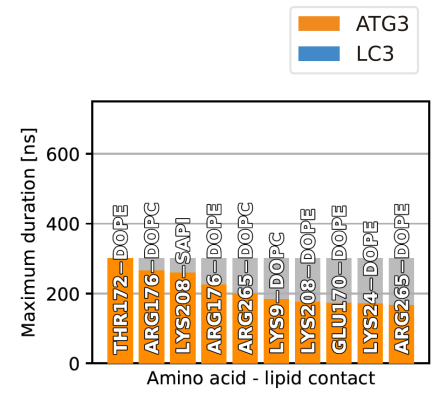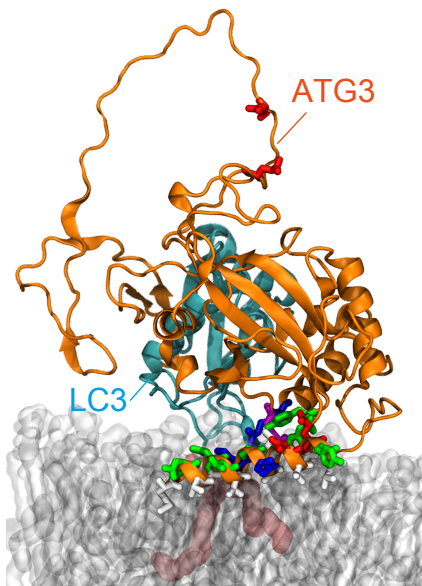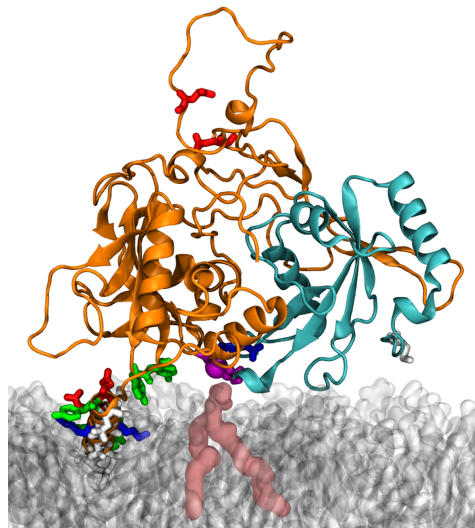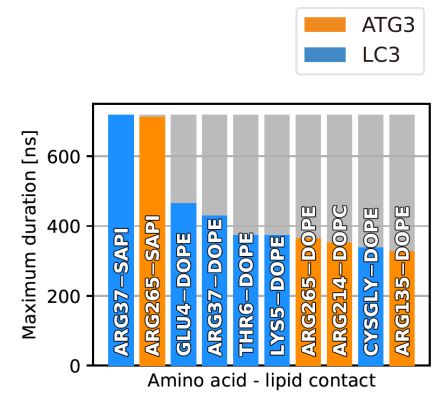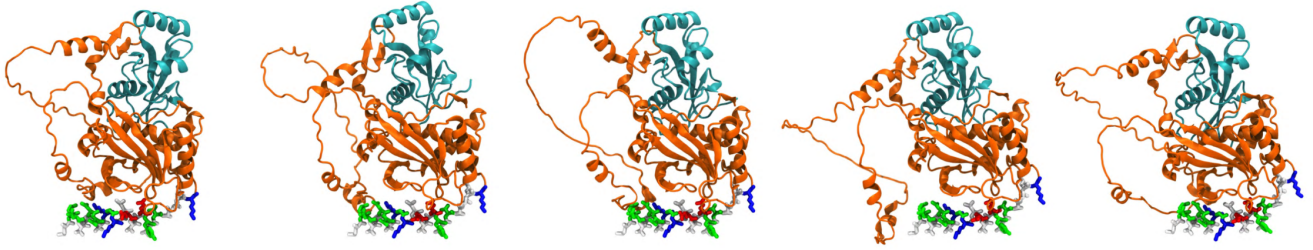
Figure 4

Figure 4. The ATG3~LC3 conjugate interacts with the membrane in MD simulations.
(**A**, **B**) Renders of a representative configuration of the ATG3~LC3 conjugate in the "LC3-UP/Disordered-DOWN" conformation. (**A**) Side view, with the ATG3 N-terminus on the left, and (**B**) axial view, with the terminal part of the AH$_{ATG3}$ closer to the viewer. The renders show the complex in a cartoon representation based on its secondary structure, with ATG3 in orange and LC3 in cyan. The atoms of residues 1-24 (AH and linker), L61, K62, K208, Y209, P263, C264 of ATG3, and M1, K42, F119, G120 of LC3 are also shown explicitly in a licorice representation. The lipid bilayer is shown in transparent gray material. Water and ions are not shown for convenience. (**C**) Histogram of the 10 longest-lasting protein-lipid contacts formed in the "LC3-UP/Disordered-DOWN" conformation. Orange indicates contacts formed between an amino acid of ATG3 and lipid head groups. (**D, E**) Renders of a representative configuration of the ATG3~LC3 conjugate in the "LC3-DOWN/Disordered-UP" conformation. Rendering and colors as in (**A**, **B**). A PE lipid forming a long-lasting contact with C264 of ATG3 is highlighted in burgundy. (**F**) Histogram of the 10 longest-lasting protein-lipid contacts formed in the "LC3-DOWN/Disordered-UP" conformation. Cyan indicates contacts formed between an amino acid of LC3 and lipid head groups.
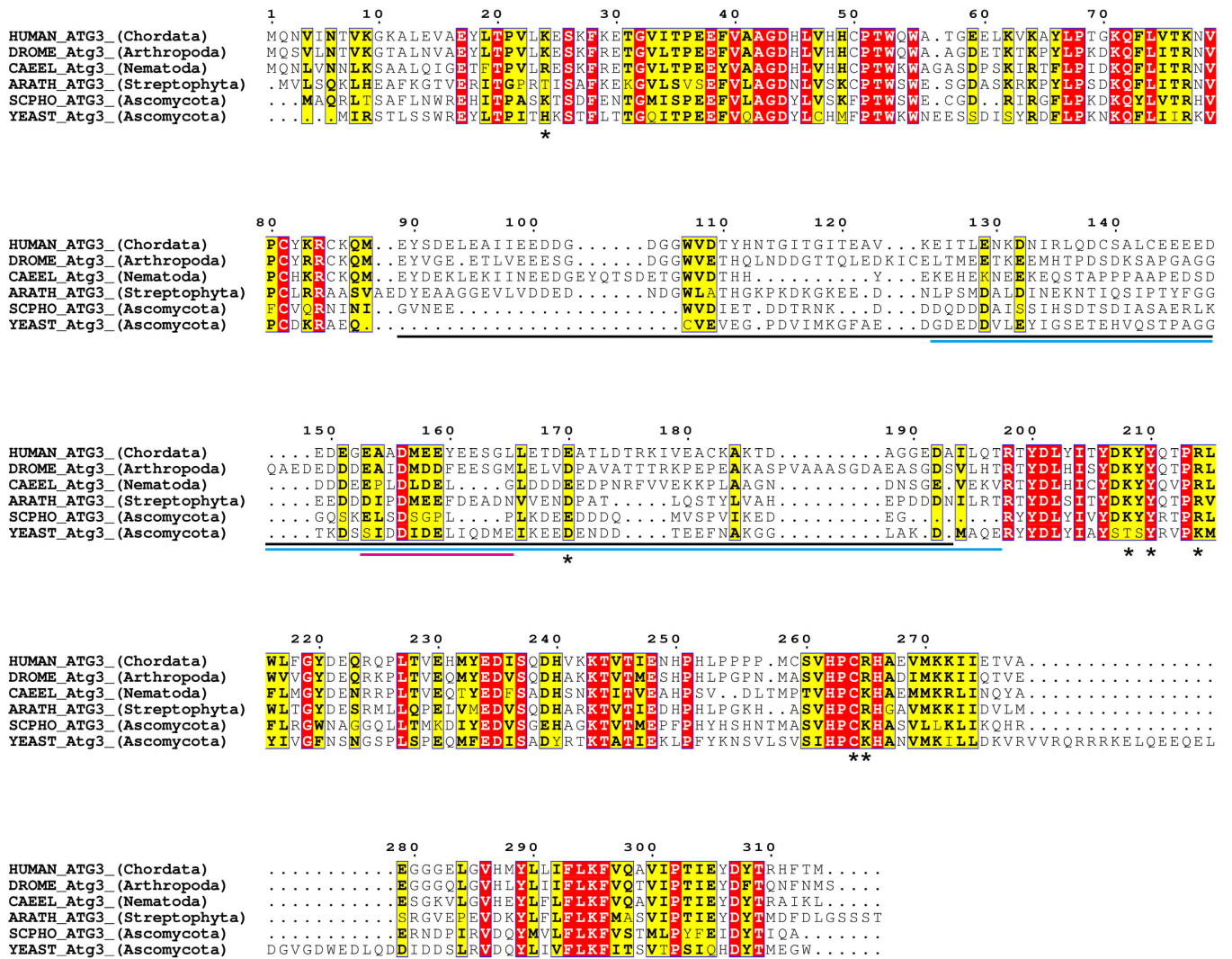
See also Figure S4.

A

B
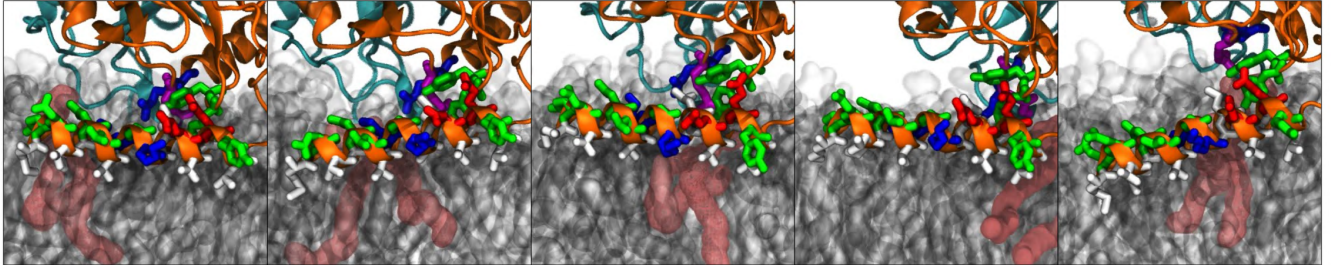
C

Figure S4

Figure S4 related to Figure 4. Alpha Fold models and AH$_{ATG3}$ dynamics in the bilayer. (**A**) Five alternative initial models of the ATG3~LC3 conjugate produced by Alpha Fold. The renders show the complex in a cartoon representation based on its secondary structure, with Atg3 in orange and LC3 in cyan. The atoms of residues 1-24 (AH and linker) are also shown explicitly in a licorice representation. (**B**) Renders of representative snapshots from a trajectory illustrating the dynamics of the ATG3 AH in the bilayer. Rendering and colors as in (**A**). Lipids are showing in transparent grey. A PE lipid forming a contact with LC3 is highlighted in burgundy. (**C**) Sequence alignment of ATG3 proteins using ESPript 3. The identical and similar residues are highlighted by red and yellow boxes, respectively. The flexible region, unfolded region and ATG12-binding region are indicated by black, cyan and magenta lines, respectively. Asterisks show the position of lipid-binding residues *in silico*.
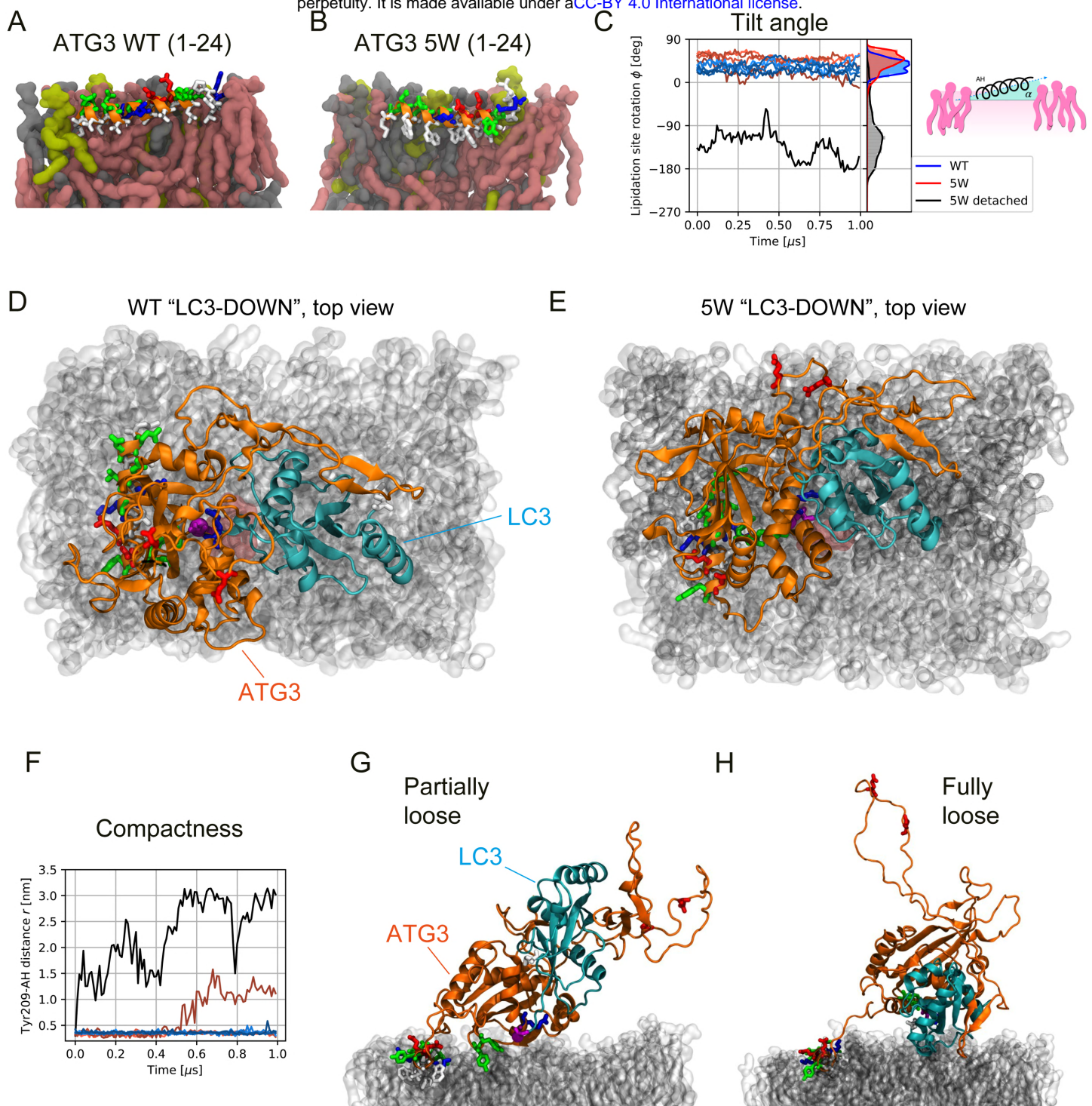
Figure 5

Figure 5. The 5W AH mutant hinders interactions between LC3 and the membrane.
(**A, B**) Renders of representative molecular configurations of the (**A**) WT AH of ATG3 and (**B**) 5W mutant. The secondary structure and residues of the AH are shown as an orange cartoon and licorice residues, respectively. The renders show a cross-section of the bilayer leaflet where the AHs are inserted. The bilayer contains the same amount of PE, PI, and PC lipids, shown in burgundy, yellow, and gray, respectively. Water and ions are not shown for clarity. (**C**) Time series of the tilt angle alpha formed by the AH in a lipid bilayer. The cartoon inset shows a definition of alpha. Blue and red indicate the values for the WT and 5W mutant, respectively. The right part of the plot reports a histogram of the two title angles.   (**D, E**) Top-view renders of two representative configurations of the ATG3~LC3 conjugate in the "LC3-DOWN" conformation, for (**A**) the WT and (**B**) the 5W mutation. The renders show the complex in a cartoon representation based on its secondary structure, with ATG3 in orange and LC3 in cyan. The atoms of residues 1-24 (AH and linker), L61, K62, K208, Y209, P263, C264 of ATG3, and M1, K42, F119, G120 of LC3 are also shown explicitly in a licorice representation. Both conformations are oriented in the same way, with the AH inserted in the bilayer on the left along the vertical direction from the C-terminus (bottom) to the N-terminus (top). The lipid bilayer is shown in transparent gray material. Water and ions are not shown for convenience. (**F**) Time series of the ATG3~LC3 conjugate compactness as measured by the distance between TYR209 and the AH. The plot shows 10 time series coming from five simulations of the WT complex and further five simulations of the 5W complex. The black and burgundy curves come from the 5W simulations. Representative conformations adopted by the 5W ATG3~LC3 conjugate corresponding to the burgundy (**G**) and black (**H**) curves in (**F**), respectively. Rendering and colors as in (**D, E**).
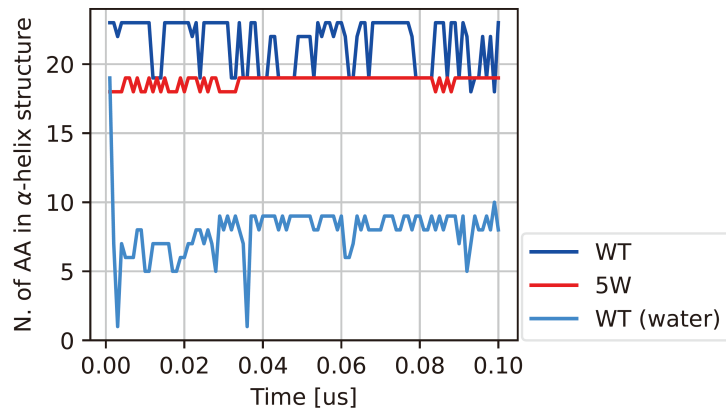
See also Figure S5.

Figure S5

Figure S5 related to Figure 5. Stability of the AH and compactness of the ATG3~LC3 conjugate

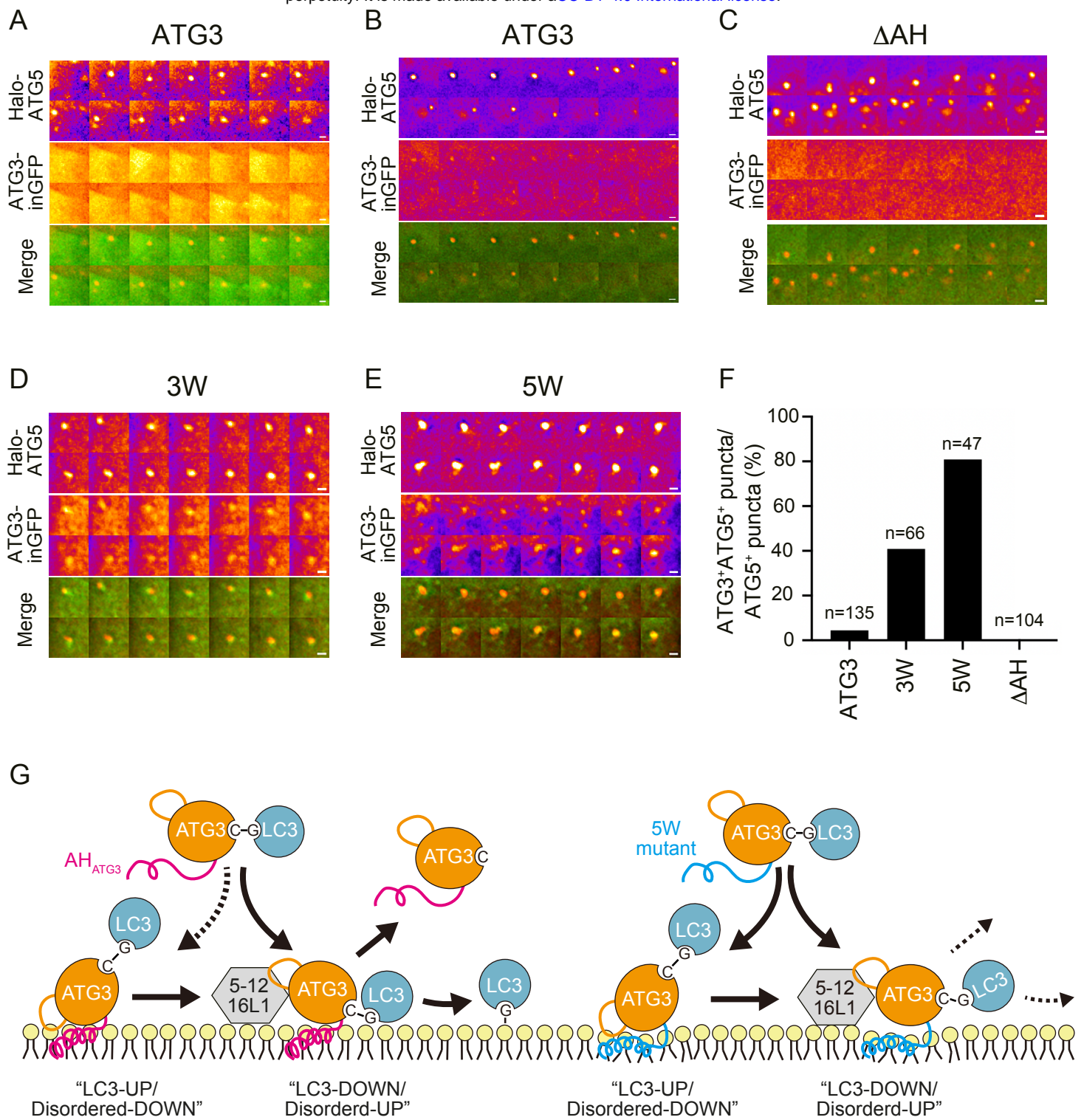Time series of the number of AH amino acids that are helical for WT and 5W in bilayer, and for WT in water.

Figure 6

Figure 6. Dynamic behavior of ATG3 on autophagic membranes depends on less bulky-hydrophobic AH.

(**A, B**) Live imaging analysis of ATG3-inGFP and Halo-ATG5 under starved condition. The cells were cultured in starvation medium with 200 nM Halo-SaraFluor 650T ligand and observed using a DeltaVision microscopy system. Frames were captured every 30 s. Images are represented in fire lookup table. Two representative images of ATG3 WT are shown. ATG3 was uniformly distributed in the cytoplasm all the time during ATG5 showed a punctate structure (**A**), while an enrichment of ATG3 signal was observed on ATG5 punctum in some cells (**B**). (**C-E**) Representative images of ΔAH deletion mutant (**C**), hydrophobic ATG3 mutants, 3W (**D**) and 5W (**E**). Scale bars, 1 μm. (**F**) Quantification of ATG3- and ATG5-double positive structures in live imaging analysis. (**G**) A speculative model for AH_{ATG3}-dependent ATG3 enzymatic reaction. [left] ATG3~LC3 conjugate is recruited to the membranes via AH_{ATG3}. When the disordered region points downwards, LC3 stays away from the membranes (LC3-UP/ Disordered-DOWN). Once the disordered region points upwards and binds to ATG12, the GLY-CYS thioester bond can get access to PE lipids, followed by LC3 lipidation and ATG3 leaving from the membranes (LC3-DOWN/ Disordered-UP). [right] ATG3~LC3 conjugate carrying 5W mutation in AH_{ATG3} is stably associated with the membranes irrespective of its interaction with ATG12. 5W mutation interferes with the organization and/or stability of ATG3~LC3 conjugate in the LC3-DOWN conformation, resulting in less LC3 lipidation.

See also Movies 1-5.

Table S1. Constructs used in this study

REAGENT or RESOURCE	SOURCE	DESCRIPTIONS
Recombinant DNA		
TN427 _ATG3 pMRX-IP-hATG3$_{1-125}$-EGFP-hATG3$_{126-314}$	This study	Retrovirus infection
TN588_V8K pMRX-IP-hATG3$_{1-125,\ V8K}$-EGFP-hATG3$_{126-314}$	This study	
TN587_ΔAH pMRX-IP-Met-hATG3$_{19-125}$-EGFP-hATG3$_{126-314}$	This study	
TN560_ATG3 chimera carrying AH$_{Spo20}$ pMRX-IP-Met-AH$_{Spo20}$-hATG3$_{19-125}$-EGFP-hATG3$_{126-314}$	This study	
TN559_ATG3 chimera carrying AH$_{NUP133}$ pMRX-IP-Met-AH$_{NUP133}$-hATG3$_{19-125}$-EGFP-hATG3$_{126-314}$	This study	
TN558_ATG3 chimera carrying AH$_{VPS34}$ pMRX-IP-Met-AH$_{VPS34}$-hATG3$_{19-125}$-EGFP-hATG3$_{126-314}$	This study	
TN561_ATG3 chimera carrying AH$_{ATG14L}$ pMRX-IP-Met-AH$_{ATG14L}$-hATG3$_{19-125}$-EGFP-hATG3$_{126-314}$	This study	
TN562_ATG3 chimera carrying AH$_{ATG2A}$ pMRX-IP-Met-AH$_{ATG2A}$-hATG3$_{19-125}$-EGFP-hATG3$_{126-314}$	This study	
TN554_ATG3 chimera carrying AH$_{DmATG3}$ pMRX-IP-Met-AH$_{DmATG3}$-hATG3$_{19-125}$-EGFP-hATG3$_{126-314}$	This study	
TN557_ATG3 chimera carrying AH$_{ScATG3}$ pMRX-IP-Met-AH$_{ScATG3}$-hATG3$_{19-125}$-EGFP-hATG3$_{126-314}$	This study	
TN556_ATG3 chimera carrying AH$_{SpATG3}$ pMRX-IP-Met-AH$_{SpATG3}$-hATG3$_{19-125}$-EGFP-hATG3$_{126-314}$	This study	
TN614_ATG3 chimera carrying AH$_{ATG2A-m1}$ pMRX-IP-Met-AH$_{ATG2A(F1758V/F1761V/W1766V)}$-hATG3$_{19-125}$-EGFP-hATG3$_{126-314}$	This study	
TN586_4A pMRX-IP-hATG3$_{1-125,\ K9A/K11A/E14A/E17A}$-EGFP-hATG3$_{126-314}$	This study	
TN595_NTQ-A pMRX-IP-hATG3$_{1-125,\ Q2A/N3A/N6A/T7A}$-EGFP-hATG3$_{126-314}$	This study	

TN617_8A pMRX-IP-hATG3$_{1-125, Q2A/N3A/N6A/T7A/K9A/K11A/E14A/E17A}$-EGFP-hATG3$_{126-314}$	This study	Retrovirus infection
TN583_3W pMRX-IP-hATG3$_{1-125, I5W/V8W/V15W}$-EGFP-hATG3$_{126-314}$	This study	
TN596_2W pMRX-IP-hATG3$_{1-125, V4W/V8W}$-EGFP-hATG3$_{126-314}$	This study	
TN603_5W pMRX-IP-hATG3$_{1-125, V4W/V8W/A12W/V15W/A16W}$-EGFP-hATG3$_{126-314}$	This study	
TN834_Halo-ATG5 pMRX-IPU-HaloTag7-mATG5	This study	

Movie 1. Live-cell time-lapse images of ATG3-inGFP and Halo-ATG5 under starved condition.

Movie 2. Live-cell time-lapse images of ATG3-inGFP and Halo-ATG5 under starved condition.

Movie 3. Live-cell time-lapse images of ATG3ΔAH-inGFP and Halo-ATG5 under starved condition.

Movie 4. Live-cell time-lapse images of ATG3(3W)-inGFP and Halo-ATG5 under starved condition.

Movie 5. Live-cell time-lapse images of ATG3(5W)-inGFP and Halo-ATG5 under starved condition.